CYCLONE GLOBAL NAVIGATION SATELLITE SYSTEM (CYGNSS)

Algorithm Theoretical Basis Document **Calibrated Raw IF based L1 Data Product**	UM Doc. No.	148-0417
	SwRI Doc. No.	N/A
	Revision	Rev 1
	Date	22 February 2024
	Contract	NNL13AQ00C

CYCLONE GLOBAL NAVIGATION SATELLITE SYSTEM (CYGNSS)

Algorithm Theoretical Basis Document	UM Doc. No.	148-0417
Calibrated Raw IF based L1 Data Product	SwRI Doc. No.	N/A
	Revision	Rev 1
	Date	22 February 2024
	Contract	NNL13AQ00C

Prepared by: Hugo Carreno Luengo   Date: 02/22/2024

Approved by: _____

Chris Ruf, CYGNSS Principal Investigator   Date: 6/24/2024

Approved by: _____
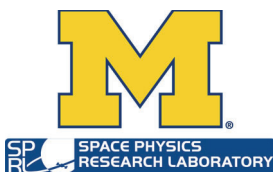
Anthony Russel, CYGNSS SOC Manager   Date: 6/24/2024

Released by: _____

Darren McKague, CYGNSS UM Project Manager   Date: 6/24/2024

REVISION NOTICE

Document Revision History		
Revision	**Date**	**Changes**
INITIAL RELEASE	20 March 2024	n/a

Contents

1   Summary

A new Cyclone Global Navigation Satellite System (CYGNSS) data product is described which is generated from the raw Intermediate Frequency (IF) data. The product includes several established signal coherence detectors, including the power-ratio P_{ratio}, complex zero-Doppler delay waveform and full entropy E_{full}, and a novel fast entropy detector E_{fast}. Both entropy detectors are provided with two temporal resolutions: 2 ms and 50 ms. Coherence performance is characterized using the phase derivative of the reflected signal at the peak of the delay waveform φ_{peak}. Threshold values of the full entropy detector are determined which classify scattering into three regimes: incoherent, partially coherent, and coherent. Several scattered signal strength products are included: Signal-to-Noise Ratio SNR, reflected power P_g, reflectivity Γ, and Normalized Bistatic Radar Cross-Section $NBRCS$. Each of these products is derived using a coherent integration time of T_c = 1 ms and incoherent integration times of N_{inc} = 1000, 500, 250, 100, 50, and 2 ms. Signal strength time series at the shorter (2 and 50 ms) times provides excellent detection of land-water transitions in heterogeneous scenes. Delay Doppler Maps (DDMs) are also generated with high delay ($\Delta\tau$ = 1/16 chip) and Doppler (Δf = 50 Hz) resolution. The behavior of each signal strength product as a coherence detector is examined using the full entropy method as a reference. Performance is characterized using Receiver Operating Characteristic (ROC) curves. The fast entropy method, which has much lower computational cost, is similarly characterized. This suite of coherence detection methods can be used to detect the presence of small inland water bodies.

2   Introduction

The CYGNSS mission [1,2] is the first micro-satellite constellation by National Aeronautics and Space Administration (NASA). CYGNSS provides high spatio-temporal sampling capabilities for Earth's science studies using Earth's surface reflected Global Positioning System (GPS) L-band signals at Left Hand Circular Polarization (LHCP). The mission was originally proposed to further advance extreme weather predictions with a focus on Tropical Cyclones (TCs) inner core process studies. More recently, the mission scientific goals were extended for land surfaces studies, including Soil Moisture Content (SMC) determination e.g. [3,4], surface water monitoring e.g. [5-7], and Freeze/Thaw (F/T) detection e.g. [8]. The CYGNSS Global Navigation Satellite Systems Reflectometry (GNSS-R) e.g. [9-16] mission team has developed several L1, L2, and L3 nominal products, which are publicly available through the NASA's Physical Oceanography Distributed Active Archive Center (PODAAC).

Additionally, CYGNSS captures raw IF signal tracks e.g. [17-19] over specific Earth's surface areas (Fig. 1). The main foundation of this CYGNSS raw IF calibrated product is on the generation of improved quality high-resolution DDMs with shorter integration times, using all the available raw IF tracks collected over land surfaces. This multi-resolution product is here made publicly available. It offers a unique opportunity for studies dedicated to e.g. river width [20], river slope [21], wetlands [22], floods [23], single pass SMC retrievals [24], and development and validation of new GNSS-R scattering models e.g. [25,26]. This scenario also offers the possibility to test and develop new GNSS-R opportunities in preparation for the Muon Space constellation, and future European Space Agency (ESA) HydroGNSS 2 micro-satellites mission [27], which is focused on land surface studies and plans to include an on-board coherent channel to continuously collect peak-DDM complex data and raw IF tracks over areas of interest.
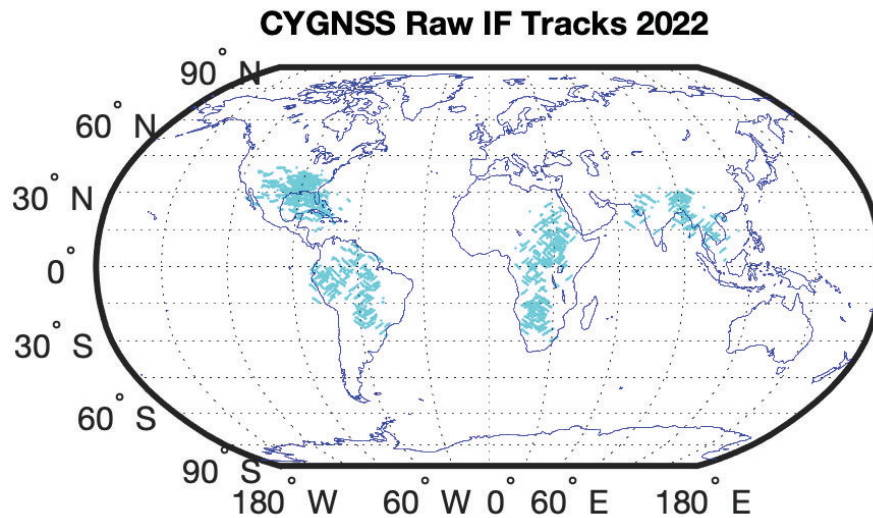
Fig. 1. Geo-distribution of the 2022 CYGNSS Earth's land surface raw IF tracks. Target areas cover mainly tropical rainforests regions as well as Southern USA, Sudan, India, and Vietnam. Specific sites were selected by the CYGNSS Science Team based on scientific requirements for on-going and future investigations.

Earth's surface water monitoring is probably one of the most promising applications of GNSS-R missions because of their high spatio-temporal sampling capabilities, and the high spatial resolution under the coherent scattering regime. This is an important research question, and it deserves further investigation. Theoretically, the resolution is limited by the size of the first Fresnel zone, with a non-negligible influence of higher order zones e.g. [28-32]. It was found that short N_{inc} provide a reasonable trade-off between an acceptable along-track spatial resolution and a reduced signal noise level, which enables to detect land-water transitions accurately [33]. We encourage the users to investigate this, and additional research questions, to further advance our understanding on the ultimate capabilities of GNSS-R. To do so, the product is delivered with a wide variety of observables [34], such as power DDMs (P_g, Γ, and $BRCS$), including the corresponding information at the peak p, as well the Normalized Bistatic Radar Cross-Section $NBRCS$, and a wide variety of coherence detectors i.e. complex delay waveforms, φ_{peak}, P_{ratio}, E_{full}, and E_{fast}. Additionally, quality flags (Appendix) and a comprehensive set of metadata e.g. Moderate Resolution Imaging Spectroradiometer (MODIS) land cover type, multi-resolution Pekel water masks, and topographic roughness are included.

This document is organized as follows. First, we introduce the CYGNSS raw IF data in Section 3. Then, the raw IF signal processing is presented in Section 4, describing the details of the enhanced DDMs, the signal calibration approach, and the derived land surface observables. Then, the coherence detectors are presented and described in Section 5. Finally, Section 6 concludes this document.

3 CYGNSS Raw IF Data

3.1 Introduction

The raw IF samples collected by the Delay Doppler Mapping Instrument (DDMI) on-board CYGNSS contain the highest possible resolution over delay and Doppler space. The access to this raw IF data enables high-resolution processing on-ground, in many ways not possible in real-time by the instrument. For example, the raw IF samples can be processed to extract in-phase I and quadrature Q information of the complex DDMs for high-quality evaluation of coherent Earth's surface scattering. Additionally, comprehensive studies of the received reflected signal power can be performed using variable delay and Doppler spacing and integration times, thus permitting the generation of extremely high-resolution DDMs for advanced science applications, including ocean and land.

3.2 Baseline L1 Mission Product

After the antenna and the Low Noise Amplifier (LNA), the GPS signal enters the on-board receiver, where it is down-converted and digitized. These raw IF samples are then processed using a Fast Fourier Transform (FFT) technique, implemented in the receiver. The real-time output is a DDM with 128 delay bins at 1/4 chip delay steps and 20 Doppler bins at 500 Hz steps. The scattered signal power is processed using a coherent integration time T_c = 1 ms and an incoherent averaging time N_{inc} = 1000 ms (December 2016-July 2019) or 500 ms (July 2019-Present). This on-board full DDM is compressed to meet the satellite downlink requirements. The compressed DDM includes 17 delay bins and 11 Doppler bins which are centered at the on-board estimated nominal specular point, and the bit depth of each bin is truncated from 32 to 8 bits. A more precise geolocation of the nominal specular point is performed on-ground. These DDMs are generated in raw uncalibrated units and calibration is performed at The University of Michigan (UMich) [35].

3.3 Raw IF Data Collection

Starting in 2017, some few raw IF datasets are being collected by the DDMI and downloaded to ground for improved studies over specific target areas, with specific interest for the CYGNSS Science Team. More recently, a new raw IF data collection strategy was approved in Winter 2022, so that ~ 20 raw IF tracks are downloaded continuously every week. Two files for each raw IF data collection are generated: one raw IF metadata file and one raw IF data file. The raw IF metadata file (Tables 1-5) contains the ID of the spacecraft, a single Data Recorder Track 0 (DRT0) packet and one or more Pulse Per Second (PPS) packets. The raw IF data file includes three sets of raw signal sample streams (~ 60 s) received by the zenith antenna, and the nadir antennas at port and starboard. All raw IF tracks collected by the CYGNSS mission to date include byte interleaved data from all three antenna channels of the DDMI, numbered as follows: zenith navigation antenna, nadir starboard side science antenna, and nadir port side science antenna.

All samples for all channels are saved as 2-bit values and are interleaved (Table 6). The source of the binary raw IF data is byte 9 through byte N of the File Transfer Packet Data (FD00) packets emitted by the DDMI. The raw IF file contains bytes 9-N of multiple contiguous FD00 packets. The FD00 packets are expected to contain consecutive sequence byte numbers. If a missing FD00 packet is detected, 2048 zero bytes are inserted in the raw IF file in place of the missing data. The first FD00 packet in the stream carries a DRT0 header block at the beginning of the data bytes. The rest of this first packet and all subsequent packets contain the binary raw IF sample data.

4 Raw IF Signal Processing

4.1 Introduction

The bandwidth of the raw signal is ~ 2.5 MHz, centered at the IF of ~ 3.8 MHz. In the nominal mode, the IF signals are sampled with a sampling rate of ~ 16.0 MHz and a resolution of 2 bits per sample, for both direct and reflected channels. The ground-based raw IF processing uses a delay-domain FFT technique to perform the correlations at all the delay samples using a frequency domain multiplication. The delay sampling is configured based on decimation of the sampling rate, and the Doppler processing range. N_{inc} and the delay-Doppler sampling properties are also configured depending on the Earth's surface type i.e. ocean vs. land. The raw IF processing is designed and built on a Linux Ubuntu laptop using the GNU Compiler Collection (GCC) compiler and the FFTW library. The code is written in C with the FFT processing based on the open source "fastgps" signal acquisition processor [36], upgraded to accept the CYGNSS raw IF data format as well as perform GNSS-R specific processing tasks, including variable non-coherent integration.

Table 1. Raw IF metadata file contents.

Bytes	Description	Notes
0	Spacecraft SCID from SwRI document 17790-ObsID, Observatory Unique Identifier Specification	0xF7: CYGNSS1 0xF9: CYGNSS2 0x2B: CYGNSS3 0x2C: CYGNSS4 0x2F: CYGNSS5 0x36: CYGNSS6 0x37: CYGNSS7 0x49: CYGNSS8 0x00: end to end simulator 0x0E: engineering model 0x0D: default
1-35	DRT0 packet	
36-83	First PPS table	
84-N	Additional PPS tables	

Table 2. Data Recorder Track 0 (DRT0) packet.

Bytes	Description	Notes
0-3	Packet Type ASCII DRT0	Four ASCII chars
4-5	GPS weeks at start	Weeks since Jan 6 1980, unsigned integer
6-9	GPS seconds at start	Second of the week, unsigned integer
10	Data format	
11-14	Sample rate	Unsigned integer, Hz
15	Channel 0: Front-end selection	
16-19	Channel 0: LO frequency	Unsigned integer, Hz
20	Channel 1: Front-end selection	
21-24	Channel 1: LO frequency	Unsigned integer, Hz
25	Channel 2: Front-end selection	
26-29	Channel 2: LO frequency	Unsigned integer, Hz
30	Channel 3: Front-end selection	
31-34	Channel 3: LO frequency	Unsigned integer, Hz

Table 3. Pulse Per Second (PPS) packet.

Bytes	Description	Notes
0-7	GPS seconds of last PPS	GPS seconds of week, double
8-11	Tick 0 sample index (PPS tick)	Unsigned integer
12-15	Tick 0 sample index	Unsigned integer
16-19	Tick 1 sample index	Unsigned integer
20-23	Tick 2 sample index	Unsigned integer
24-27	Tick 3 sample index	Unsigned integer
28-31	Tick 4 sample index	Unsigned integer
32-35	Tick 5 sample index	Unsigned integer
36-39	Tick 6 sample index	Unsigned integer
40-43	Tick 7 sample index	Unsigned integer
44-47	Tick 8 sample index	Unsigned integer

Table 4. Data format.

Value	Data format	Description	ADC Precision
0	Channel 1, I only	Records data from source into data recorder channel 1, sampling I only	2 bit (sign-mag)
1	Channel 1,2 I only	Records data from source into data recorder channel 1, and 2, sampling I only	2 bit (sign-mag)
2	Channel 1,2,3 I only	Records data from source into data recorder channel 1,2, and 3, sampling I only	2 bit (sign-mag)
3	Channel 1,2,3,4 I only	Records data from source into data recorder channel 1,2,3, and 4 sampling I only	2 bit (sign-mag)
4	Channel 1, I and Q	Records data from source into data recorder channel 0, sampling I and Q	2 bit (sign-mag)

Table 5. Front-end selection.

Value	Description
1	RF 1- MAX2769 (zenith antenna)
2	RF 2- MAX2769 (starboard antenna)
3	RF 3- MAX2769 (port antenna)
4	RF 4- MAX2769 (unimplemented)

Table 6. FD00 packet.

Bytes	Description	Notes
0	SpW target logical address	Unsigned integer
1	SpW protocol ID	Unsigned integer
2-5	Packet type ASCII FD00	Unsigned integer
6-7	Packet length-length of data excluding all header bytes	Unsigned integer
8	Sequence byte	Unsigned integer
9	Data byte 0, binary raw IF data	Unsigned integer
10	Data byte 1	Unsigned integer
11	Data byte 2	Unsigned integer
…	…	Unsigned integer
N	Last data byte	Unsigned integer

4.2 Multi-Resolution Enhanced DDMs

Different types of enhanced DDMs can be generated to improve and enable new scientific applications over land and ocean by CYGNSS (Table 7). The main three DDM types are illustrated in Fig. 2. In so doing, the key parameters are the following: coherent integration time T_c, incoherent integration time N_{inc}, delay bin resolution $\Delta\tau$, Doppler bin resolution Δf, delay window d_w , and Doppler window D_w. This document is focused on Earth's land surfaces (Fig. 2a).

All enhanced DDMs are generated with Δf = 50 Hz Doppler bin resolution and $\Delta\tau$ = 1/16 chip delay bin resolution. The DDMI estimation of the Doppler at the nominal specular point is introduced in the raw IF processing to reproduce as much as possible the on-board scenario for calibration purposes. The DDMI Doppler information is provided every N_{inc} = 1000 ms (December 2016-July 2019) or every N_{inc} = 500 ms (July 2019-Present). A spline method is applied to the DDMI-based Doppler vector to generate more precise Doppler inputs for lower integration times N_{inc} = 250 ms, N_{inc} = 100 ms, N_{inc} = 50 ms, and N_{inc} = 2 ms.

The delay bin resolution is determined by the effective sampling rate. In the nominal mode, raw IF data are sampled at a rate of ~ 16 MHz, which is approximately 16000 samples per 1 ms. Approximately, 16 samples per GPS Coarse/Acquisition (C/A) code chip is a delay chip resolution of 1/16 chip in the DDMs. The raw IF processing allows the selection of different delay bin resolutions, so that the ~ 16 MHz samples are down-sampled:

• 1/8 chip delay bin resolution: Down-sampling by a factor of 2 to a ~ 8 MHz sampling rate or 8 samples per chip.

• 1/4 chip delay bin resolution: Down-sampling by a factor of 4 to a ~ 4 MHz sampling rate or 4 samples per chip.

• 1/2 chip delay bin resolution: Down-sampling by a factor of 8 to a ~ 2 MHz sampling rate or 2 samples per chip, which is the Nyquist limit for the GPS C/A code

(a)   (b)   (c)
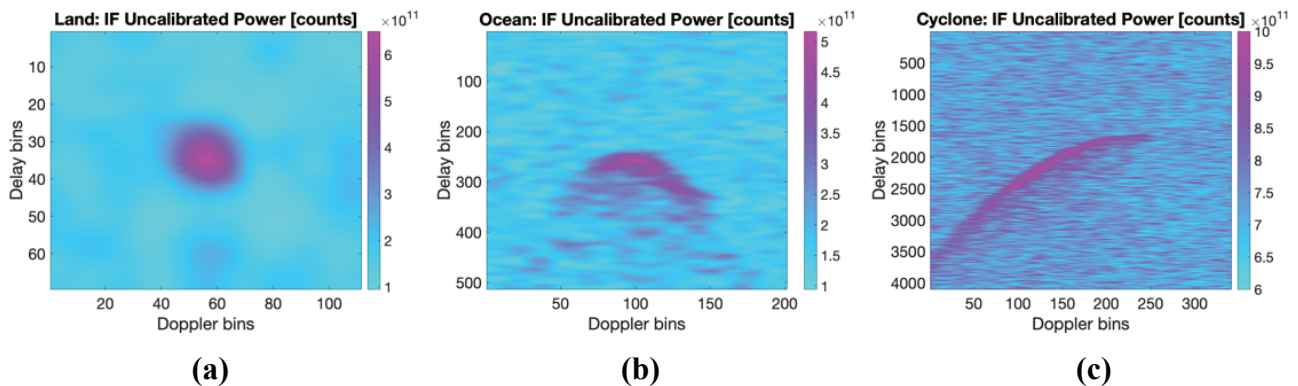
Fig. 2. Enhanced uncalibrated DDMs [Δf = 50 Hz Doppler bin resolution, $\Delta\tau$ = 1/16 chip delay bin resolution] derived from the raw IF processing in counts: (a) Standard DDM - Land (N_{inc} = 50 ms), (b) Full DDMs - Ocean (N_{inc} = 50 ms), (c) Super DDMs - Cyclone (N_{inc} = 250 ms). The antenna footprint on the surface often truncates one side of the signal (Fig. 2c).

Table 7. Summary of the properties of each raw IF data product type. This document is focused on land. Coherent integration time T_c, incoherent integration time N_{inc}, delay bin resolution $\Delta\tau$, Doppler bin resolution Δf, delay window d_w , and Doppler window D_w.

	T_c [ms]	N_{inc} [ms]	$\Delta\tau$ [chips]	Δf [Hz]	d_w [bins]	D_w [bins]
Land	1	1000, 500,250, 100, 50,2	1/16	50	69	111
Ocean	1	1000, 500,250, 100,50	1/16	50	513	201
Cyclone	1	1000, 500, 250	1/16	50	4097	401

The output power after raw IF processing is not exactly the same at different delay sampling rates because the processing uses 1 ms FFTs in each case on different length vectors to perform the correlations. The shorter the vector the faster the FFT, but delay samples are thrown out. The highest achievable resolution, which has the slowest FFTs, is at the full sampling rate or 16 samples per chip (i.e. 1/16 chip delay bin resolution). As such, the use of 1/16 chip delay bin resolution without sample decimation provides the highest fidelity results. The required longer run time is not a limiting consideration because the processing is performed on-ground.

The raw IF processing output DDMs are generated in raw uncalibrated units, known as counts (Fig. 2). There is a scale difference between these DDMs and those generated by the DDMI probably due to the on-board compression algorithm and the fact that the DDMI uses the "Zoom" Doppler domain correlator (and possibly some internal, unknown, bit overflow shifting/scaling) [37]. This difference must be compensated. Additionally, both processing chains must be referenced to the GPS absolute time. Thus, before radiometric calibration, time synchronization and scaling strategies must be defined.

4.3 Time Synchronization and Geolocation

Accurate GPS timing information derived from the direct signal received by the zenith navigation antenna is used to improve the geolocation of the nominal specular point over the Earth's surface. The nominal specular point position is computed over the World Geodetic System (WGS) 84 ellipsoid of reference and then the solution is projected over the NASA Shuttle Radar Topography Mission (SRTM) global digital elevation model. This improvement as compared to the nominal mission data enables more accurate land-surfaces studies. Original data strategy was designed for ocean wind speed retrieval for long N_{inc}, and the on-board timing precision is adequate to that goal.

Additionally, a lag-correlation technique is used for each Pseudorandom Noise (PRN) code number, to align the on-board generated time series and the raw IF based time series, before calibration. Lag-correlation is the correlation between two series where one of the series has a time lag with respect to the other. This is required to compensate for a variable temporal offset that is present between the two time series. The compensation of this offset is used to align the raw IF time series with the on-board operations in real-time processing. Time series at different N_{inc} are aligned at the beginning of each sampling rate's integration period.

4.4 Calibration Strategy

4.4.1 Scaling

Uncalibrated DDMs are measured in counts. These counts are linearly related to the total signal power generated by the raw IF processing (C_{if}) or the DDMI (C_{ddmi}).

Raw IF based DDMs (C_{if}) in counts can be related to the arriving signal power as follows:

$$C_{if}(\tau, f) = G_{if}(P_a + P_r + P_g(\tau, f) + P_e) \tag{1}$$

where τ is delay, f is Doppler, G_{if} is the end-to-end gain of the raw IF processor, P_a is the thermal noise power generated by the antenna (in watts), P_r is the thermal noise power generated by the instrument (in watts), P_g is the scattered GNSS power (in watts), and P_e (in watts) represents certain parameters of the real time signal processing performed by the DDMI on orbit which are unknown, and so cannot be exactly duplicated by the ground processing of raw IF data.

DDMI based DDMs (C_{ddmi}) in counts can be related to the arriving signal power as follows:

$$C_{ddmi}(\tau, f) = G_{ddmi}(P_a + P_r + P_g(\tau, f)) \tag{2}$$

where G_{ddmi} is the end-to-end gain in the real time DDMI processing.

Combining eqn. 1 and eqn. 2, both types of uncalibrated DDMs can be linearly related as follows:

$$C_{ddmi}(\tau, f) = \left(\frac{G_{ddmi}}{G_{if}}\right) C_{if}(\tau, f) - G_{ddmi}P_e \tag{3}$$

The first step in the calibration is to estimate the coefficients to transform $C_{if}(\tau, f)$ in $C_{ddmi}(\tau, f)$:

$$p_1 = \frac{G_{ddmi}}{G_{if}} \tag{4}$$

and

$$p_2 = -G_{ddmi}P_e \tag{5}$$

After lag-correlation, a linear regression between the times series (Fig. 3) at the maximum peak (subscript p) of the raw IF based ($C_{if,p}$) and the DDMI based DDMs ($C_{ddmi,p}$) at N_{inc} = 500 ms is used (Fig. 4) to empirically determine the coefficients for each PRN code number per channel. This is necessary because certain parameters of the real time signal processing performed by the DDMI on orbit are unknown and so cannot be exactly duplicated by the ground processing of raw IF data. These parameters include the start and stop times of the coherent correlation relative to the time varying phase of the GPS L1 carrier signal and the phase tracking algorithm used to synchronize the timing of the correlator. Both parameters can affect the scaling of the DDM data products.

The scale factor is derived with the corresponding high delay and Doppler bin resolution raw IF time series [Δf = 50 Hz, $\Delta\tau$ =1/16 chip], because the output power of the raw IF processor is different at different delay sampling rates. Additionally, the impact of different N_{inc} is considered. The output reflected power changes with different N_{inc} since the software processing computes an accumulation over the incoherent integration time. It does not compute an average over the incoherent integration time. So, there is a need to scale linearly with the length of the integration interval as follows (Fig. 5):

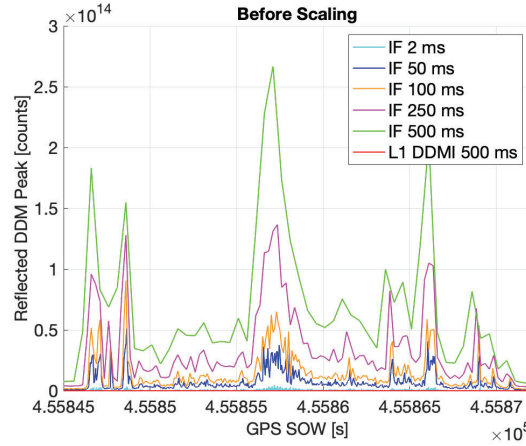$$C_{if,scaled,N_{inc}}(\tau, f) = p_1 C_{if,N_{inc}}(\tau, f)\frac{N_{inc,0}}{N_{inc}} + p_2 \tag{6}$$

Fig. 3. Before-scaling comparison of DDMI [$\Delta f = 500$ Hz, $\Delta \tau = 1/4$ chip, $N_{inc} = 500$ ms] and raw IF [$\Delta f = 50$ Hz, $\Delta \tau = 1/16$ chip] peak reflected-power time series [counts]. These time series correspond to a single PRN number within one raw IF file. Track acquired on 22/4/2022. The DDMI L1 (red) trace is so low it seems to be a flat zero as its 10^5 vs 10^{14} for the raw IF (see Fig. 5 for trend after scaling).
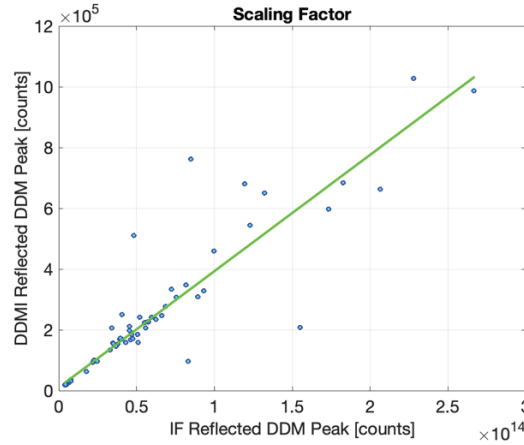

Fig. 4. Sample scale factor between DDMI [$\Delta f = 500$ Hz, $\Delta \tau = 1/4$ chip, $N_{inc} = 500$ ms] and the $N_{inc} = 500$ ms raw IF [$\Delta f = 50$ Hz, $\Delta \tau = 1/16$ chip] time series of reflected peak power in raw uncalibrated units [counts] after lag-correlation. This sample scale factor corresponds to a single PRN number within one raw IF file. Track acquired on 22/4/2022.

where N_{inc} is any incoherent averaging, and $N_{inc,0}$ is the incoherent averaging time used to derive the scale factor $(p1, p2)$ i.e. 500 ms after July 2019. It is worth to highlight that the scale factor (p1, p2) is derived for each raw IF track.

Fig. 5 shows the after-scaling time series. The output reflected power of the different time series is un-biased. Additionally, the raw IF time series show a higher dynamic range and an improved resolution as compared to the DDMI because of the shorter integration times down to $N_{inc} = 2$ ms, and the higher delay and Doppler bin resolution [$\Delta f = 50$ Hz, $\Delta \tau = 1/16$ chip].

After scaling, the Signal-to-Noise Ratio SNR is computed as follows:

$$SNR = 10 log10 \left(\frac{C_{if,p,scaled,N_{inc}}}{C_{N,if,scaled,N_{inc}}} \right) \tag{7}$$

where $C_{N,if,scaled,N_{inc}}$ is the noise power. Noise information is calculated separately for each DDM, using pixels where no signal power is present i.e. the 180 top delay rows of the original uncompressed 512 x 200 DDMs [$\Delta f = 50$ Hz, $\Delta \tau = 1/16$ chip] in counts.
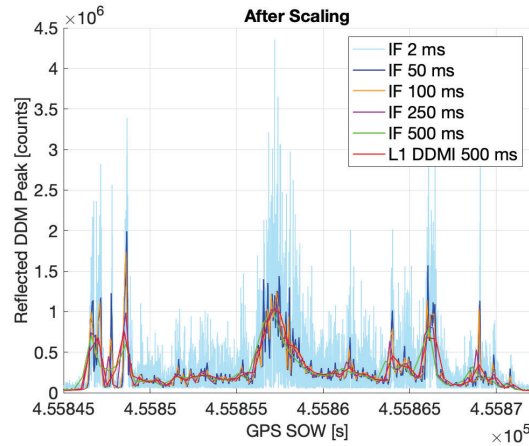
Fig. 5. After-scaling comparison of DDMI [Δf = 500 Hz, $\Delta\tau$ = 1/4 chip, N_{inc} = 500 ms] and raw IF [Δf = 50 Hz, $\Delta\tau$ = 1/16 chip] peak reflected-power time series [counts]. These time series correspond to a single PRN number within one raw IF file. Track acquired on 22/4/2022.
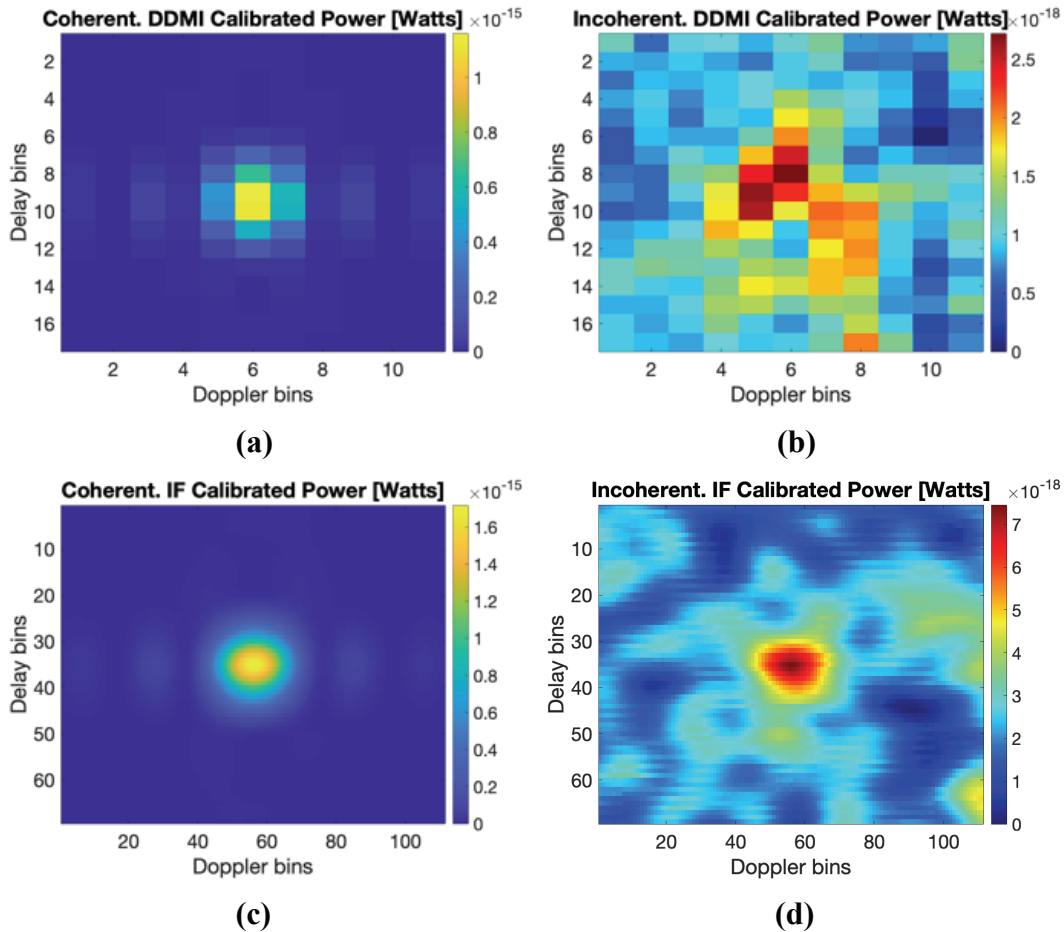

Fig. 6. Sample DDMs: (a)-(b) standard L1 DDMI data [Δf = 500 Hz, $\Delta\tau$ = 1/4 chip, N_{inc} = 500 ms] and (c)-(d) raw IF calibrated product [Δf = 50 Hz, $\Delta\tau$ = 1/16 chip, N_{inc} = 50 ms] for (a)-(c) coherent scattering regime and (b)-(d) incoherent scattering regime.
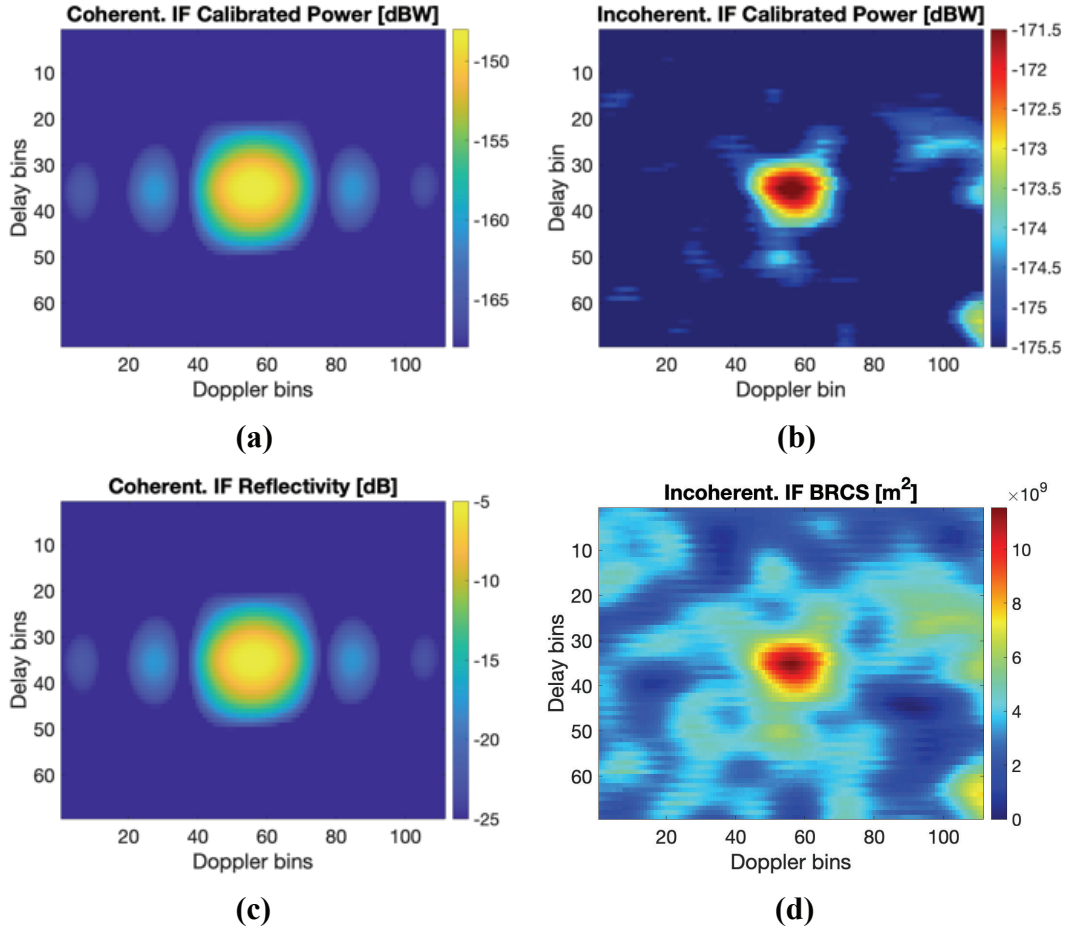
Fig. 7. Raw IF sample DDMs [Δf = 50 Hz, $\Delta \tau$ = 1/16 chip, N_{inc} = 50 ms] under the coherent scattering regime (a)-(c), and the incoherent scattering regime (b)-(d): (a) $P_g(\tau, f)$, (b) $P_g(\tau, f)$, (c) $\Gamma(\tau, f)$, and (d) $BRCS(\tau, f)$.

4.4.2 Radiometric Calibration

This section describes the radiometric calibration [38-40] approach used to convert each bin of the after-scaling DDMs in counts $C_{if,scaled,N_{inc}}(\tau, f)$ to units of watts $P_g(\tau, f)$. After radiometric calibration, the reflected power DDMs (in watts) are derived as follows (Fig. 6):

$$P_g(\tau, f) = \frac{C(P_B + P_r)}{C_B} \tag{8}$$

where $C = (C_{if,scaled,N_{inc}}(\tau, f) - C_{N,if,scaled,N_{inc}})$, P_B is the blackbody thermal noise power, and C_B is the DDM in the blackbody state.

The DDM noise power is expressed in counts as:

$$C_{N,if,scaled,N_{inc}} = p_1 C_{N,if,N_{inc}} \frac{N_{inc,0}}{N_{inc}} + p_2 \tag{9}$$

where $C_{N,if,N_{inc}}$ is the noise of the before-scaling DDMs.

P_B and C_B are derived on-board during the blackbody calibration, when a calibration switch selects between the nadir antenna and a blackbody target as the source of the input signal to the DDMI. The blackbody calibration is performed every 60 s (before August 2021) for each nadir antenna. The DDM in the blackbody state is as follows:

$$C_B = G(P_B + P_r) \tag{10}$$

P_B can be expressed as follows:

$$P_B = kT_I B_w \tag{11}$$

where T_I is the effective temperature of the instrument blackbody load source. P_B is determined from a physical temperature sensor measured at 1 Hz and is near enough in time to the 1 Hz science measurement, so that the physical temperature does not change significantly between the thermistor reading and the science measurement. C_B is made within 10 min (starting in August 2021) of science measurement, and close enough in time, so that the receiver gain, and noise figure do not change significantly [41]. Additionally, the blackbody measurements are on-ground re-sampled and interpolated to the measurement time.

The thermal noise power generated by the DDMI can be expressed as follows:

$$P_r = kT_r B_w = k[(NF - 1)290]B_w \tag{12}$$

where NF is the DDMI noise figure and T_r is the DDMI temperature. The NF vs. temperature profile was characterized pre-launch for all the instruments LNAs. The NF is continuously updated in-orbit.

4.4.3 Inverting Land Surface Parameters

Several L1b observables are derived after radiometric calibration, including reflectivity $\Gamma(\tau, f)$, Bistatic Radar Cross-Section $BRCS\ (\tau, f)$, and Normalized Bistatic Radar Cross-Section $NBRCS\ (\tau_p, f_p)$.

The reflectivity DDM is estimated as follows (Fig. 7c):
$$\Gamma(\tau, f) =$$
$$\frac{(4\pi)^2 P_g(\tau, f)(R_r(\tau_p, f_p) + R_t(\tau_p, f_p))^2}{\lambda^2 G_r(\tau_p, f_p) EIRP(\tau_p, f_p)} \tag{13}$$

where R_t and R_r are the ranges from the transmitter and the receiver to the Earth's surface scattering area, G_r is the receiver antenna gain, λ is the signal electromagnetic wavelength, and $EIRP$ is the transmitter Equivalent Isotropically Radiated Power of the Right Hand Circular Polarization (RHCP) direct GPS signal.

The Bistatic Radar Cross-Section DDM is estimated as follows (Fig. 7d):
$$BRCS(\tau, f) =$$
$$\frac{(4\pi)^3 P_g(\tau, f)(R_r(\tau_p, f_p)R_t(\tau_p, f_p))^2}{\lambda^2 G_r(\tau_p, f_p) EIRP(\tau_p, f_p)} \tag{14}$$

The surface Normalized Bistatic Radar Cross-Section is estimated as follows:
$$NBRCS(\tau_p, f_p) = \frac{BRCS(\tau_p, f_p)}{A_{eff}} \tag{15}$$

where A_{eff} is the effective scattering area corresponding to a 4 delay bins x 10 Doppler bins cell around the peak, because over land surfaces the scattered signal is concentrated in a small area near the specular point. For the inversion of the land observables, the calibration variables are approximated with the values corresponding to the peak. This is used for the calibration of the ocean DDMs (Fig. 2b) but approximating at the nominal specular point [38]. Thus, it can be applied over land surfaces because the scattering is more

specular (scattered signal is concentrated in a small area near the specular point) than over ocean. However, when the scattering is very diffuse i.e. off-specular (Fig. 2c), this approximation is no longer valid, and per-bin calibration variables must be used along the complete d_w and D_w windows (Table 7). Additionally, the delay-Doppler ambiguity introduced by the Woodward Ambiguity Function (WAF) must be considered.

### 4.4.4 Time Series Analysis: Reflectivity Case

Time series of peak reflectivity $\Gamma_p = \Gamma(\tau_p, f_p)$ are selected to highlight some product capabilities, but more observables are available for the final users. Two IF tracks are considered over a Surface Water and Ocean Topography (SWOT) mission cal/val site (Figs. 8,9) and the Pacaya-Samiria region in the Amazon basin (Figs. 10,11). The corresponding geolocation of Γ_p using Landsat imagery is depicted in Figs. 9,11. The N_{inc} = 2 ms and 50 ms Γ_p time series show a higher signal dynamic range and a higher spatial resolution than those corresponding to N_{inc} = 500 ms. There is clear evidence of the sensitivity of Γ_p to the presence of surface water, showing the capability to detect small inland water bodies (Fig. 12) and land-water transitions over complex heterogeneous scenes.

In the SWOT site, low $\Gamma_p \sim < 0.1$ levels (Fig. 8a) appear over vegetated areas because of the larger attenuation of the reflected signal by the vegetation cover [42-44] (Fig. 9a). On the other hand, in the inundated terrain located in one lateral of the Amazon River, Γ_p increases up to ~ 0.2. The Amazon River is then divided in several arms, surrounded by vegetation. Γ_p can capture sharp transitions land-water-land. Within the river, there is a combination of sharp peaks $\Gamma_p \sim 0.5$ with lower values ~ 0.2 probably because of the different surface roughness conditions across the wide Amazon River. It is worth to point out that the spatial resolution gradually decreases with increasing N_{inc}. The 500 ms Γ_p time series is not able to resolve this complex scene (Fig. 9d). On the other hand, increasing N_{inc} help to reduce signal noise e.g. N_{inc} = 2 ms vs. N_{inc} = 50 ms.

The Pacaya-Samiria scene (Fig. 11) is characterized by a complex-form river within the Amazon basin, surrounded by dense vegetation and several other small-size water bodies (Fig. 12). The orientation of the selected raw IF track is interesting because the nominal specular point crosses some of these water bodies, and additionally is laterally surrounded by a few of them. The N_{inc} = 2 ms Γ_p time series (Fig. 11a) resolves this complex scene better than longer times, showing that the spatial resolution under the coherent scattering regime is fine enough to detect small inland water bodies, while the impact of higher order Fresnel zones appears negligible is this scenario (Fig. 12). However, there is a non-negligible impact in target areas characterized by a large and smooth surface water extension surrounded by heavy-vegetation [31,32].
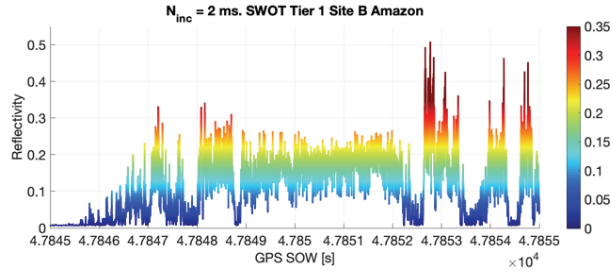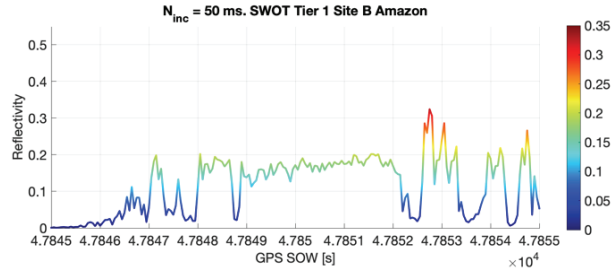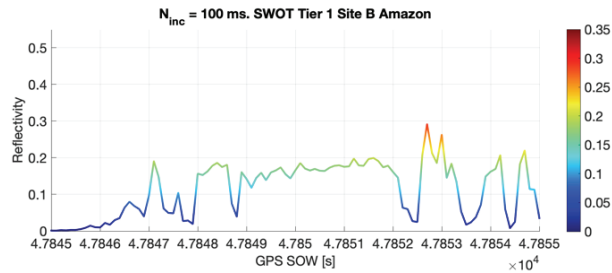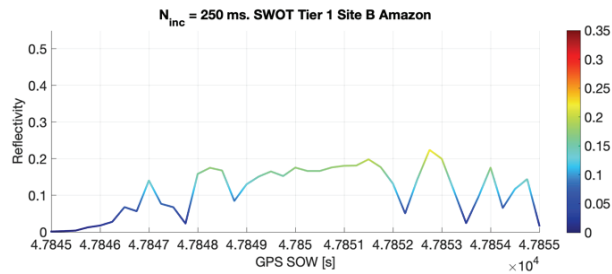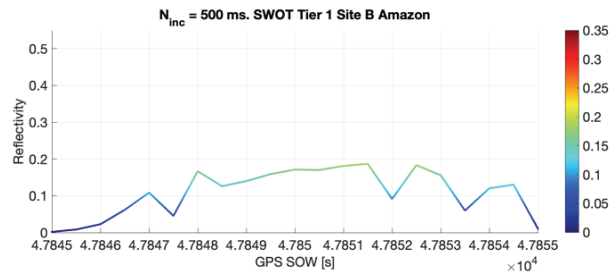
Fig. 8. GNSS-R raw IF reflectivity Γ_p time series in the SWOT cal/val site (track acquired on 3/27/2022) for N_{inc}: (a) 2 ms, (b) 50 ms, (c) 100 ms, (d) 250 ms, and (e) 500 ms.
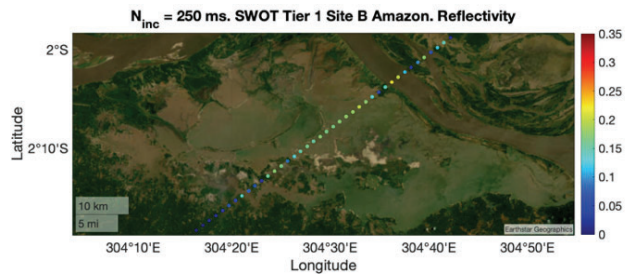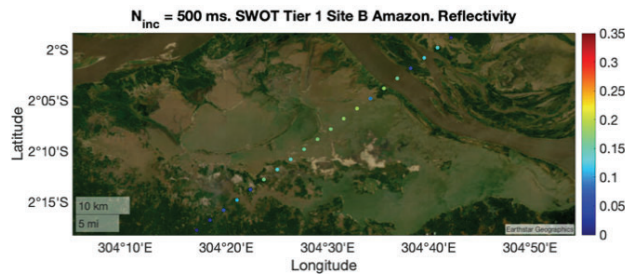
Fig. 9. GNSS-R raw IF reflectivity Γ_p geolocated in the SWOT cal/val site (track acquired on 3/27/2022) for N_{inc}: (a) 2 ms, (b) 50 ms, (c) 100 ms, (d) 250 ms, and (e) 500 ms.
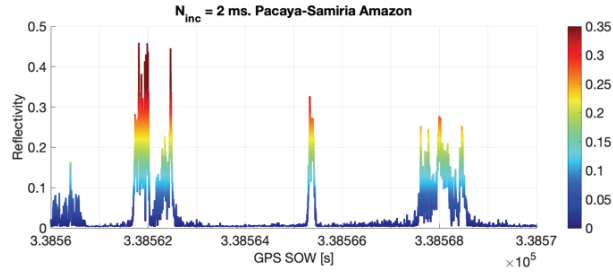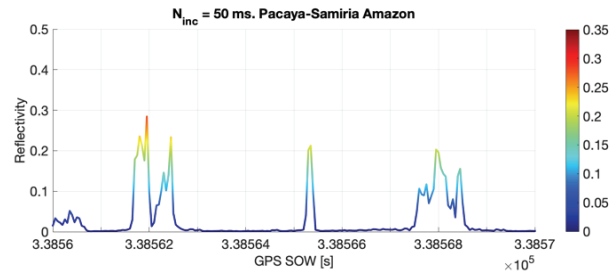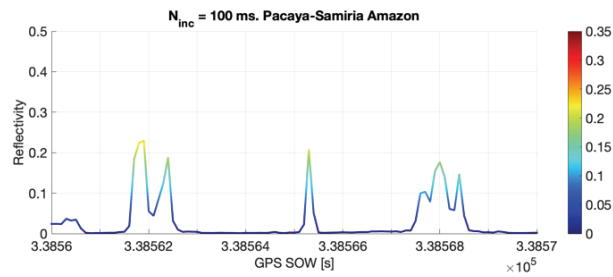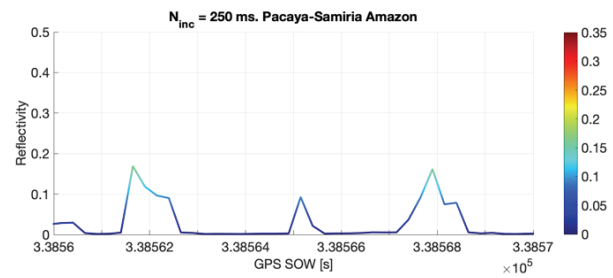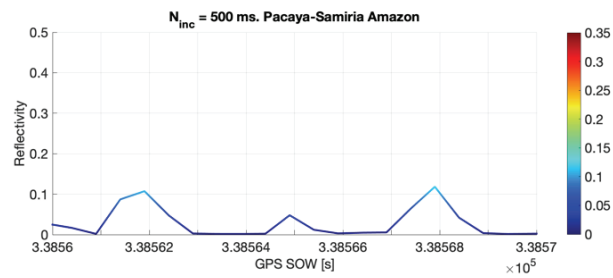
Fig. 10. GNSS-R raw IF reflectivity Γ_p time series in Pacaya-Samiria (track acquired on 16/2/2022) for N_{inc}: (a) 2 ms, (b) 50 ms, (c) 100 ms, (d) 250 ms, and (e) 500 ms.
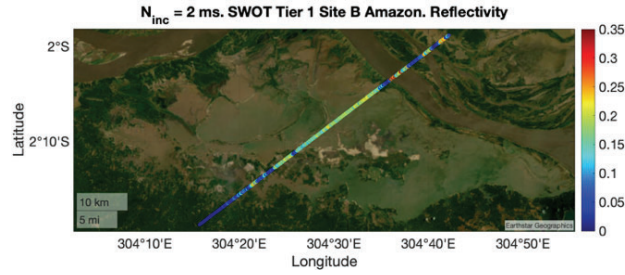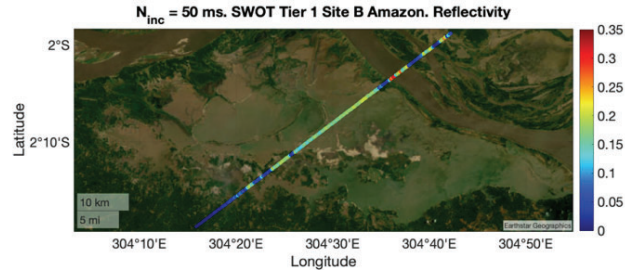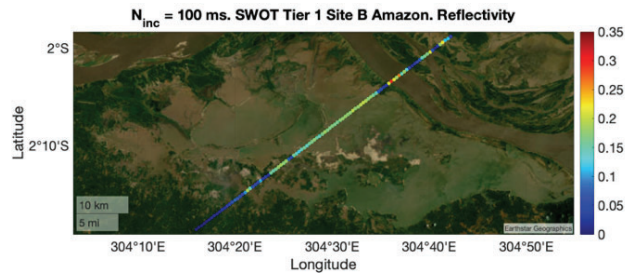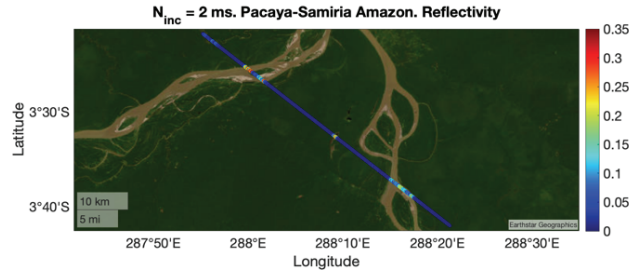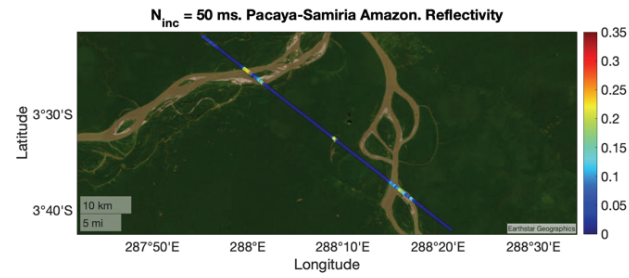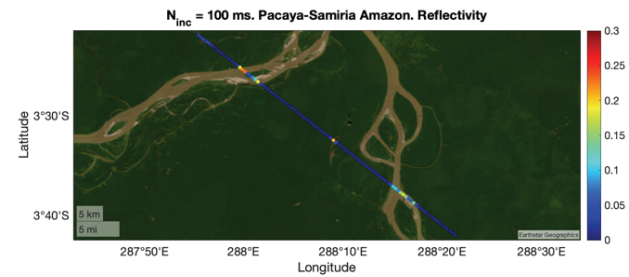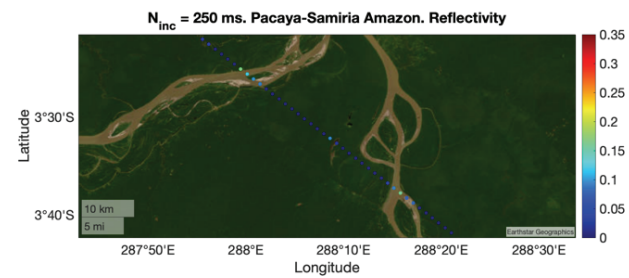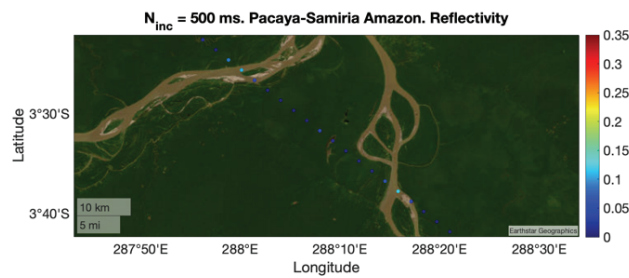
Fig. 11. GNSS-R raw IF reflectivity Γ_p geolocated in Pacaya-Samiria (track acquired on 16/2/2022) for N_{inc}: (a) 2 ms, (b) 50 ms, (c) 100 ms, (d) 250 ms, and (e) 500 ms.

(a)

(b)
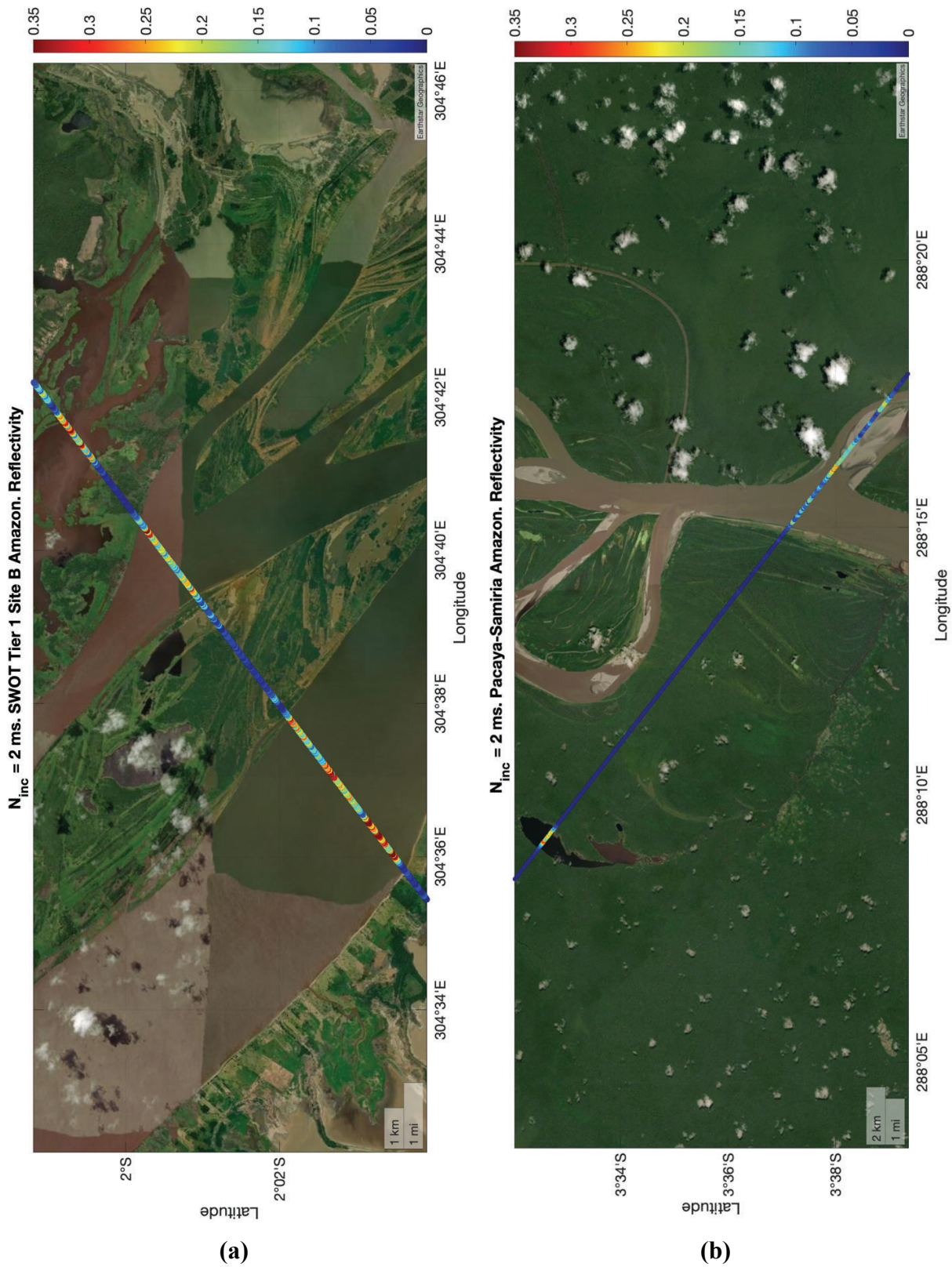
Fig. 12. Zooming GNSS-R raw IF reflectivity Γ_p over high-interest target areas: (a) Track acquired on 3/27/2022 – Fig 9.a, (b) track acquired on 16/2/2022 – Fig. 11.a. Land-water transitions are accurately captured by CYGNSS. Over water, the reflectivity increases because of the higher dielectric constant, smoother surface, and absence of vegetation cover. It is also worth to highlight that the signal fluctuations over water are probably due to variable surface roughness.

5 Coherence Detectors

5.1 Introduction: Coherent and Incoherent Scattering Modeling

There are several correlation techniques to extract the geophysical information from the scattered GNSS signals. CYGNSS uses the classical GNSS-R or cGNSS-R. The scattered electric field is cross-correlated with a replica of the known GNSS codes, so as to generate the so-called complex DDMs (Fig. 13):

$$Y(\tau, f) = \frac{1}{T_c} \int_0^{T_c} a(t)u(t+\tau)e^{2\pi j(f_c+f)t}dt \tag{16}$$

where a represents the modulating PRN code, u is the received signal, f_c is the GNSS carrier frequency, and t is the time. In a spaceborne scenario, increasing T_c is debatable as the motion of the receiver (~ 7 km/s) will limit the signal phase coherence. Some results estimated that close to $T_c = 1$ms is near optimal, $T_c \sim 0.8$ ms for a faster moving Shuttle instrument, [11] while $T_c = [1, 2]$ ms for a classical GNSS-R configuration [45]. However, since the scattered signal is of even weaker amplitude than the direct one and additionally it suffers from speckle noise, a large number of incoherent averages have to be done to improve the signal-to-noise ratio of the so-called power DDMs:

$$\langle |Y(\tau, f)|^2 \rangle = \frac{1}{N_{inc}} \sum_{i=1}^{N_{inc}} |Y(\tau, f)|^2 \tag{17}$$

Power DDMs can be modeled as the sum of two terms [13,28,32,43]:

$$\langle |Y(\tau, f)|^2 \rangle = \langle |Y_{inc}(\tau, f)|^2 \rangle + \langle |Y_{coh}(\tau, f)|^2 \rangle \tag{18}$$

where $\langle |Y_{inc}(\tau, f)|^2 \rangle$ is the incoherent scattering term and $\langle |Y_{coh}(\tau, f)|^2 \rangle$ is the coherent scattering term. $\langle |Y_{inc}(\tau, f)|^2 \rangle$ can be obtained as it follows [13]:

$$\langle |Y_{inc}(\tau, f)|^2 \rangle = \frac{\lambda^2}{(4\pi)^3} \iint \frac{EIRPG_r}{R_r^2 R_t^2} \gamma \sigma^0 |X(\tau, f)|^2 dA \tag{19}$$

where χ is the WAF, σ^0 is the bistatic scattering coefficient, γ is the transmissivity of the vegetation [44], and A is the scattering area, which is limited to the so-called glistening zone.

Under the Huygens-Kirchhoff principle, $\langle |Y_{coh}(\tau, f)|^2 \rangle$ can be expressed as [29-32]:

$$\langle |Y_{coh}(\tau, f)|^2 \rangle =$$

$$\upsilon \frac{\lambda^2 G_r EIRP}{4\pi} \left| -jk \iint \frac{2cos\theta_i X(\tau, f)}{4\pi R_t R_r} \sqrt{\gamma |R|^2 e^{-(2k\sigma cos\theta_i)^2}} e^{jk(R_t+R_r)} dA \right|^2 \tag{20}$$

where υ is is the characteristic free space wave impedance $\sim 120\pi$, k is the angular wavenumber, θ_i is the incidence angle, R is the complex Fresnel reflection coefficient, and σ is the surface height standard deviation (related to small-scale surface roughness).

Results have demonstrated the impact of higher order Fresnel zones on the total coherent reflected power as collected by a GNSS-R sensor, showing ringing fluctuations in the reflected power near high contrast boundaries. This theoretically determines the spatial resolution of the coherent scattering over heterogenous areas.

(a)   **(b)**
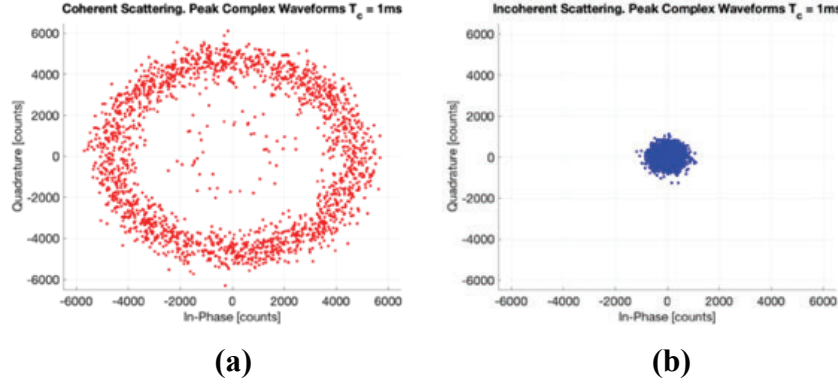
Fig. 13. Scattered complex field (peak of the complex delay waveform, $T_c = 1$ ms, no incoherent averaging): (a) Coherent scattering, (b) incoherent scattering.
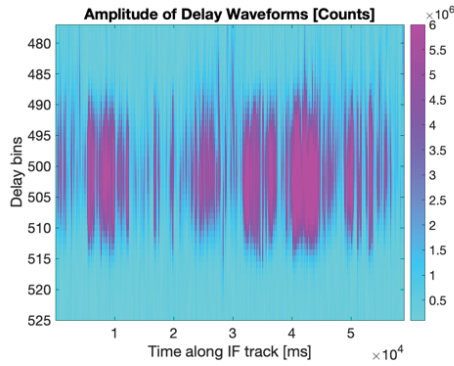
Fig. 14. Sample temporal serie of delay vector over the White River basin, AR, USA (track acquired on 15/1/2022).
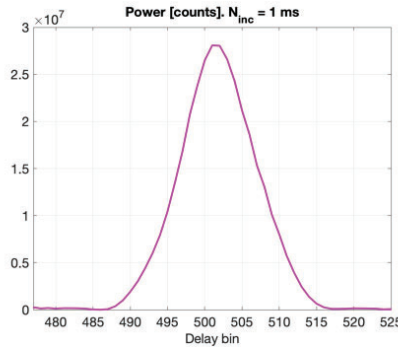
Fig. 15. Sample zero-Doppler delay waveform [$T_c = 1$ ms and $N_{inc} = 1$ ms] over the White River basin, AR, USA (track acquired on 15/1/2022).

5.2 Coherent Detector: Definitions

Several coherence indices are provided to help the final users in selecting the most appropriate observable for each targe area, depending on the dominant scattering mechanism i.e. coherent or incoherent.

The full entropy detector E_{full} is obtained applying the Von Neumann entropy definition to the corresponding GNSS-R density matrix D_{full} as follows [46]:

$$E_{full} = -Tr(D_{full} log D_{full}) \tag{21}$$

where the symbol Tr is the trace of the matrix.

The full GNSS-R density matrix D_{Full} is calculated after normalization of the eigenvalues β using its trace:

$$D_{Full} = \frac{\beta}{Tr(\beta)} \tag{22}$$

where β is the diagonal eigenvalues matrix generated with the Generalized Eigen-Decomposition (GED) of the correlation matrix Q:

$$\phi^{tp} Q \phi = \beta \tag{23}$$

where ϕ is the eigenvectors matrix and the superscript tp denotes the matrix transpose. Q is generated from the N sequential snapshots of the zero-Doppler delay waveforms Z [$T_c = 1$ ms and $N_{inc} = 1$ ms] (Figs. 14,15) as $Q = ZZ^H/N$, where H denotes Hermitian transposition. In this study, 48 bins centered at the maximum peak of the waveforms are used for entropy calculations. $Tr(\beta)$ is equal to the sum of its eigenvalues. E_{full} output values are finally generated with two different temporal resolutions 2 ms and 50 ms.

This metric uses the idea of entropy as an estimation of the information available in the eigenvalues of the correlation matrix. The eigenvalues are a reliable estimator of the energy distributed along dimensions of the signal subspace. $E_{full} \sim 1$ represents a uniform eigenvalues distribution, which is an indication of totally incoherent scattering. On the other hand, $E_{full} \sim 0$ indicates the presence of a dominant eigenvalue, which is an indication of totally coherent scattering. The full entropy E_{full} detector is based in the variations in time of the scattered signal, as well as in the shape of the waveforms.

The fast entropy detector E_{fast} is a fast and approximated calculation of E_{full}. It is computed using the Von Neumann entropy definition as follows:

$$E_{fast} = -Tr(D_{fast} \log D_{fast}) \tag{24}$$

where D_{fast} is the fast GNSS-R density matrix, which is defined as follows:

$$D_{Fast} = \frac{\eta}{Tr(\eta)} \tag{25}$$

where η is the diagonal eigenvalues matrix. η_1, is the largest eigenvalue of the correlation matrix after whitening correlated additive noise Q_w, which is computed using the so-called power method [47]. The second eigenvalue η_2 is defined as the mean value of the remaining eigenvalues. The power method is used to iteratively find the eigenvalue of Q_w that is largest in absolute value i.e. the dominant eigenvalue of Q_w. Although this restriction may seem severe, dominant eigenvalues are of primary interest in many physical applications, which is the case.

The power ratio P_{ratio} is the ratio of the raw counts of the 13 x 51 delay-Doppler grid surrounding the peak value of C_{if} [$\Delta f = 50$ Hz, $\Delta \tau = 1/16$ chip], over the sum of the rest of the values as follows [48]:

$$P_{ratio} = \frac{P_{ratio,in}}{P_{ratio,out}} \tag{26}$$

where

$$P_{ratio,in} = \tag{27}$$

$$\sum_{i=-6}^{6} \sum_{j=-25}^{25} C_{if}(\tau_p + i, f_p + j)$$

and

$$P_{ratio,out} =$$
$$\sum_{i=1}^{d_w} \sum_{j=1}^{D_w} C_{if}(i,j) - P_{ratio,in} \tag{28}$$

5.2 Time Series Analysis: Detectors Inter-Comparison

One single raw IF track over a complex heterogeneous scene in the Pacaya-Samiria region is selected to show an inter-comparison of the time series of the three coherence detectors previously described (Figs. 16-18).

The full entropy E_{full} and fast entropy E_{fast} suddenly decrease when a water body approaches the nominal specular point because the coherent scattering becomes dominant, and thus there is a dominant eigenvalue (Figs. 16, 18). Consequently, the reflectivity Γ_p increases, which is an additional indication that the surface scattering is mainly coherent $\langle|Y_{coh}(\tau,f)|^2\rangle$ over surface water bodies [28,46,48].

On the other hand, in the presence of vegetated areas, both entropy indices (E_{full} and E_{fast}) increase because the scattered signal becomes incoherent $\langle|Y_{inc}(\tau,f)|^2\rangle$. It is worth to point out that E_{full} shows more clear transitions from coherent to incoherent regimes and a higher signal dynamic range than E_{fast} (Figs. 16a,b). Additionally, the power ratio P_{ratio} time series is depicted (Fig. 18c). P_{ratio} increases in the presence of water. P_{ratio} was designed primarily for use when signal phase information is not available (i.e. the standard CYGNSS L1 products). It has been adapted for its application with short integration times and high delay and Doppler resolution DDMs by tunning the noise exclusion threshold process.

Fig. 17 shows a comparison of the full entropy coherence detector E_{full} and the 2-km resolution Pekel water mask. E_{full} provides real-time information regardless of weather conditions, while the Pekel mask is based on averaged optical Landsat imagery from the global surface water explorer [49]. This is the reason why the Pekel mask is not able to show the presence of water over areas covered by vegetation (Fig. 17), while the GED of Q enables the capability to detect small coherence changes (Fig. 17).

(a)

(b)
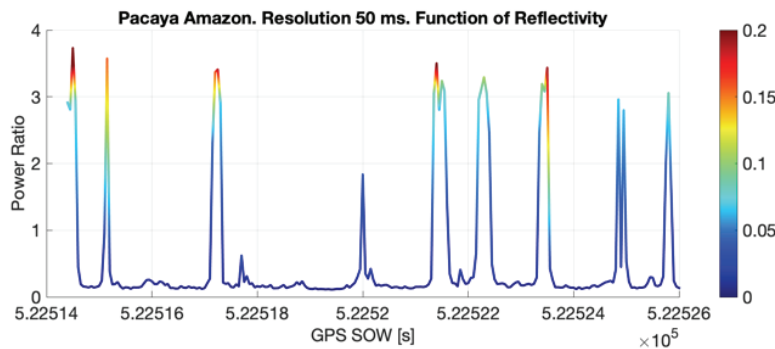
(c)

Fig. 16. Coherence detectors time series in Pacaya-Samiria (track acquired on 31/12/2022) as a function of Γ_p: (a) E_{full}, (b) E_{fast}, and (c) P_{ratio}.

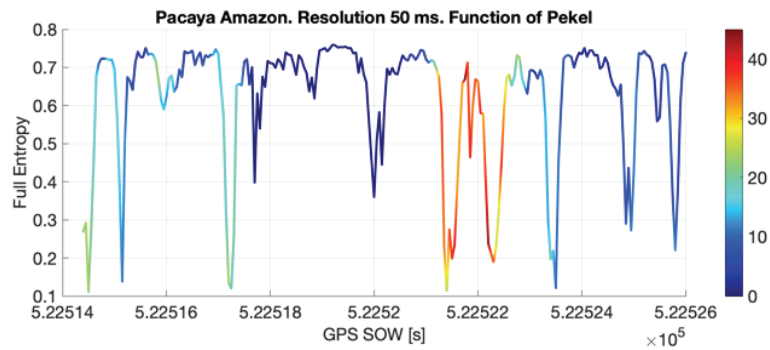Fig. 17. Comparison of the full entropy E_{full} coherence detector and the 2-km spatial resolution Pekel surface water percentage [%] over Pacaya-Samiria (track acquired on 31/12/2022).

(a)

(b)

(c)
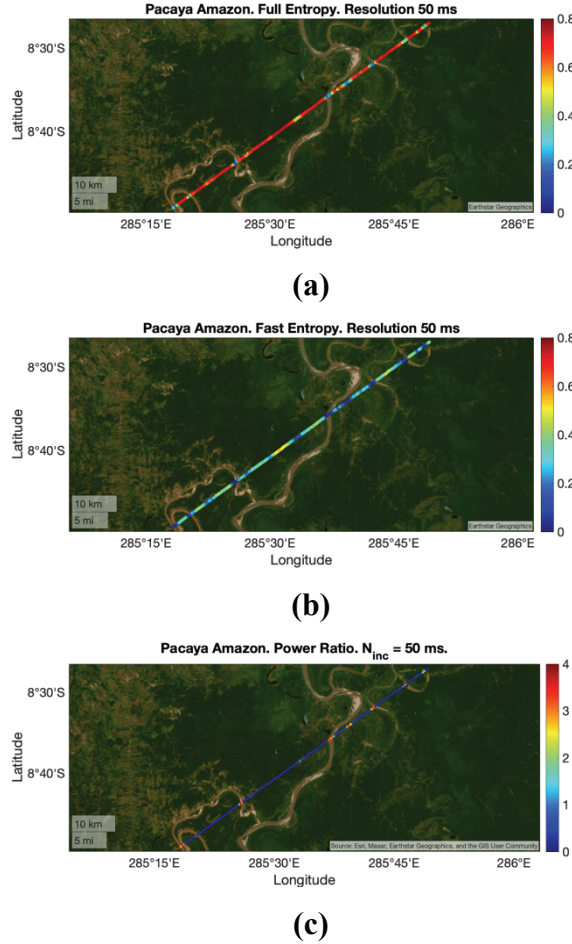
Fig. 18. Coherence detectors geolocated in the Pacaya-Samiria (track acquired on 31/12/2022) for (a) E_{full}, (b) E_{fast}, and (c) P_{ratio}.

5.3 A Full Entropy Based Coherence Classification

GNSS-R surface scattering over land surfaces is composed of two terms, coherent $\langle|Y_{coh}(\tau,f)|^2\rangle$ and incoherent $\langle|Y_{inc}(\tau,f)|^2\rangle$ scattering, depending mainly on surface roughness [50-54]. The full entropy E_{full} is the most powerful coherence detector presented in this study (Fig. 16a). Here it is selected as the main truth reference for further evaluation. The phase derivative at the peak of the reflected complex zero-Doppler delay waveforms φ_{peak} is used to derive the full entropy levels that can be used to classify the different scattering regimes. φ_{peak} is computed as the arctangent of the product of the complex peak $Y_n(\tau_p, f_p)$ and the conjugate of the previous complex peak $Y_{n-1}(\tau_p, f_p)$, with $T_c = 1$ ms.

Two raw IF tracks have been selected over target areas with differentiated geophysical properties (Fig. 19); the first one over the SWOT cal/val site (Figs. 19a,20), and the second one over the Pantanal [55,56], which is the world's largest tropical wetland area (Figs. 19b,21). Both regions are characterized by the presence of surface water covered by heavy upwelling vegetation. This scene remains unresolved for optical sensors.

Three different scattering regimes are shown in Figs. 20 and 21, including incoherent, partially coherent, and coherent. The classification is based on E_{full} time series with 50 ms of resolution, because of the noisier performance with 2 ms. The variance decreases by increasing the number of waveforms (Fig. 15) for the estimation of each entropy value. The larger the number of waveforms under consideration, the larger the heterogeneity of the equivalent footprint, but the overall entropy is lower. This is relatively similar to speckle noise mitigation by coherent averaging, which increases the coherence of the signal as compared to lower T_c.
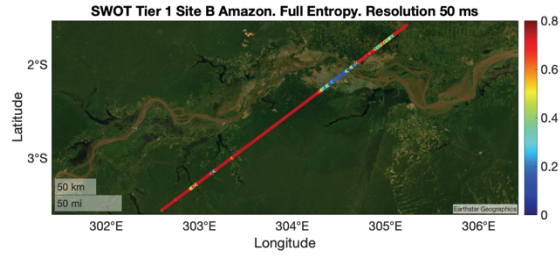
(a)
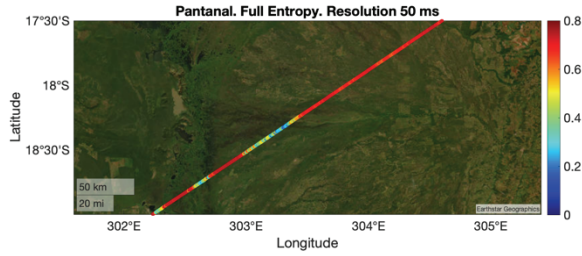
(b)

Fig. 19. E_{full} tracks geolocated in: (a) the SWOT ca/val site (track acquired on 3/27/2022) and (b) the Pantanal (track acquired on 7/7/2022) target areas.

(a)

(b)

Fig. 20. Time series in the SWOT cal/val site (track acquired on 3/27/2022): (a) φ_{peak} and (b) E_{full}. Full entropy levels are identified for classification of several scattering regimes: incoherent, partially coherent, and coherent.

Additionally, it is worth to comment that the minimum entropy levels are of the same order, independently of the number of waveforms considered for calculations. The incoherent scattering regime is characterized by random phase fluctuations and full entropy levels higher than $E_{full} \sim 0.7$. This state appears in densely vegetated areas without surface water (Fig. 19). The partially coherent regime is characterized by a noisy linear trend of the phase derivative φ_{peak} and full entropy levels between $E_{full} \sim 0.3$ and $E_{Full} \sim 0.7$. This state is found in regions such as e.g. the Pantanal wetlands (Fig. 19). Finally, the coherent scattering regime
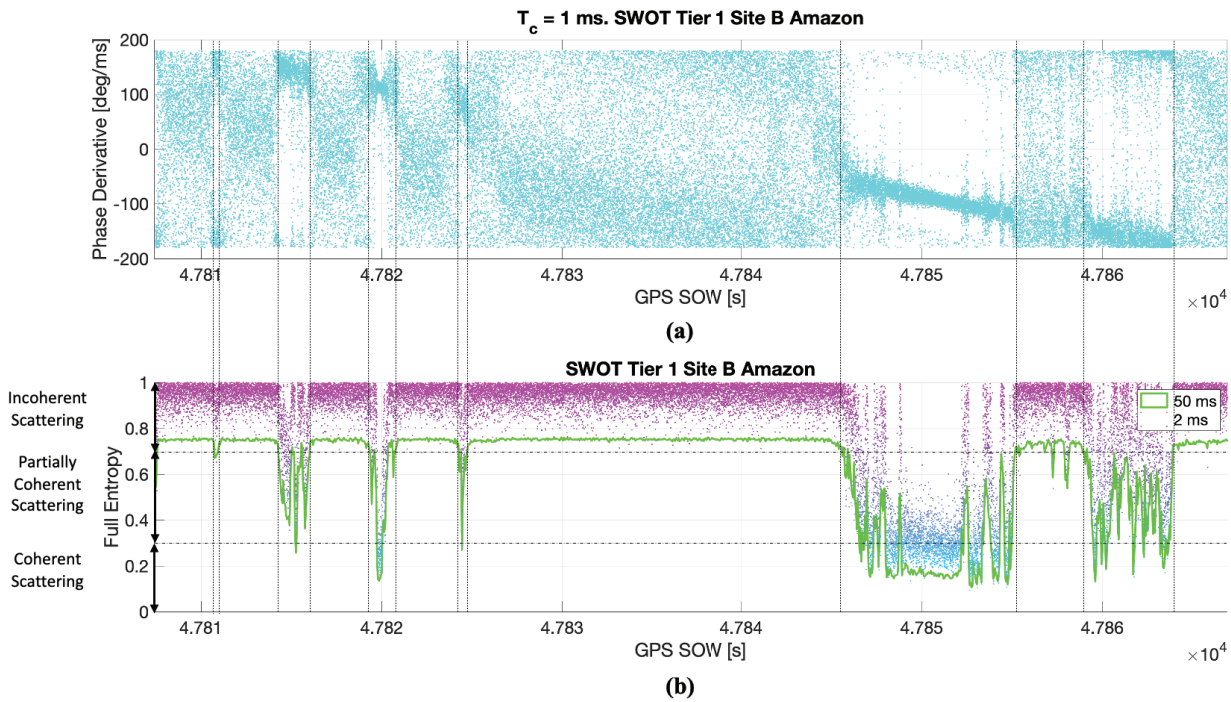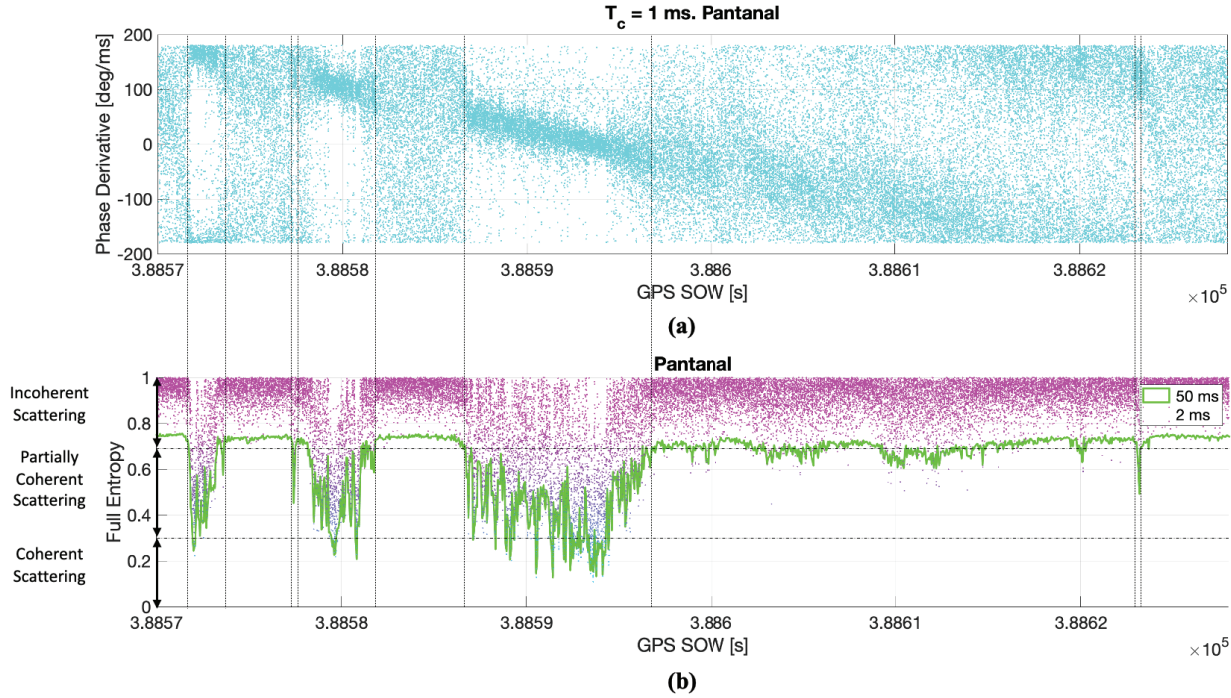
Fig. 21. Time series in the Pantanal (track acquired on 7/7/2022): (a) φ_{peak} and (b) E_{full}. Full entropy levels are identified for classification of several scattering regimes: incoherent, partially coherent, and coherent.

is found for full entropy levels below $E_{full} \sim 0.3$. φ_{peak} is clearer in this state, which is associated with the presence of inland water bodies without upwelling vegetation cover i.e. low γ levels. In this scenario, when the surface is smooth, the scattering is highly coherent, and the reflected signal phase can be tracked. This characterization has been found to provide an accurate scattering classification over the complete CYGNSS raw IF dataset. In this section, two tracks have been selected to illustrate their temporal series, and in the next section, the study is performed using the full dataset.

5.3 Full Dataset Assessment: Fast vs. Full Entropy

Finally, all the available raw IF tracks collected over land surfaces in 2022 are selected for a global scale assessment. The performance of E_{fast} vs. E_{full} is evaluated as a function of SNR (Fig. 22a), P_{ratio} (Fig. 22b), $NBRCS$ (Fig, 22c), and Γ_p (Fig. 22d). E_{fast} has a lower computational requirement (eqn. 24) than E_{full} (eqn. 21), but there is a clear functional relationship between both entropy metrics. For the coherent scattering regime i.e. $E_{full} \sim < 0.3$, the relationship appears linear, which means that E_{fast} is an excellent coherence detector, despite the use of the power method for the estimation of the dominant eigenvalue. On the other hand, it seems that E_{fast} saturates for $E_{full} \sim > 0.7$. This is probably because of the better capability of E_{full} to capture the incoherent scattering regime, and its higher signal dynamic range (Fig. 16). This improved performance is possible because of the higher accuracy of the GED in determining the eigenvalues than numerical methods. E_{fast} uses the mean value of the remaining eigenvalues, as an estimation of the second eigenvalue η_2, and thus there is a limitation in the detection of the incoherent scattering which is associated with a uniform eigenvalues distribution.

Higher values of SNR (Fig. 22a), P_{ratio} (Fig. 22b), $NBRCS$ (Fig, 22c), and Γ_p (Fig. 22d) are clustered within the coherent ($E_{full} \sim < 0.3$) and the partially coherent ($0.3 \sim < E_{full} \sim < 0.7$) scattering regimes. To further evaluate the performance of the different observables and coherence detectors, we use the ROC curves [8],
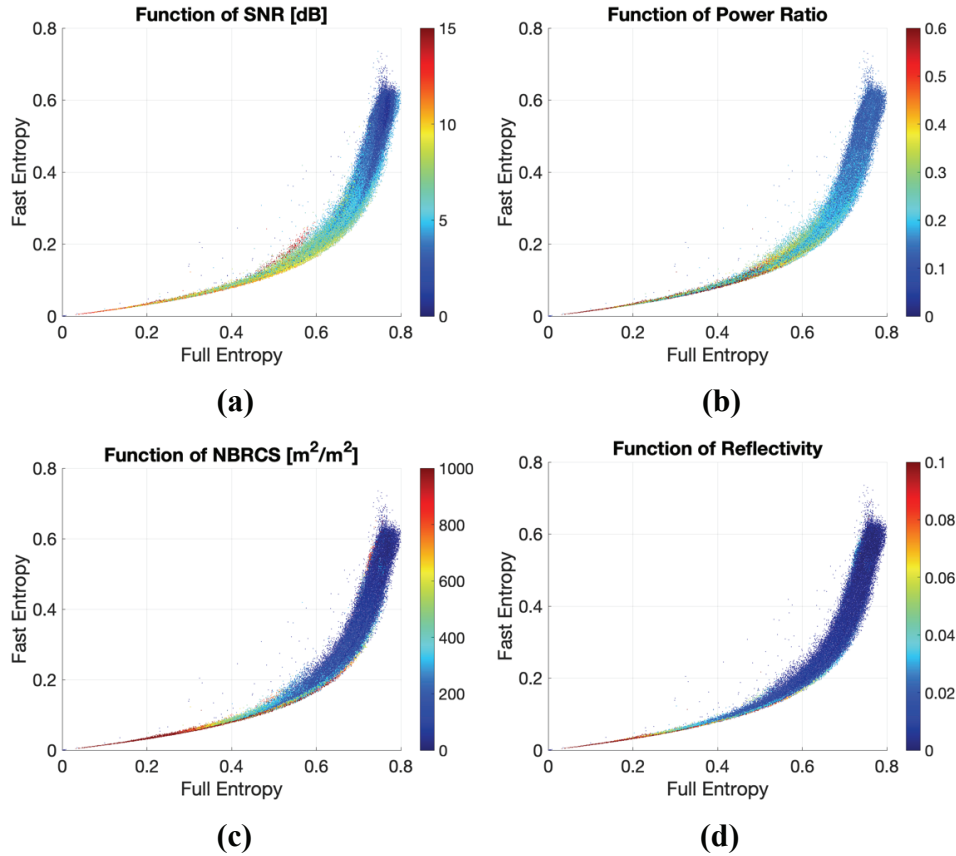
Fig. 22. Scatter plots of the E_{Fast} vs. the E_{Full} (resolution 50 ms) using all the available raw IF tracks collected over land surfaces in 2022, as a function of the following parameters with N_{inc} = 50 ms: (a) SNR, (b) P_{ratio} (c) $NBRCS$, and (d) Γ_p.

using E_{full} as proxy data (Fig. 23). The scattering is incoherent if the full entropy is $E_{full} \sim > 0.7$, and it is coherent when full entropy is $E_{full} \sim < 0.3$ (Figs. 20,21).

The optimum operating point of a ROC curve is defined at the point of inflection when the slope of each curve crosses from above to below unity (Fig. 23). This point marks the transition from more true than false detections to more false than true.

Additionally, the ratio of the Probability of Detection (PD) and the False Alarm Rate (FAR) is related to the area between each curve and the diagonal line (PD = 0 & FAR = 0 to PD = 1 & FAR = 1) in Fig. 23: E_{fast_area} (~ 0.49), SNR_{area} (~ 0.47), and P_{ratio_area} (~ 0.47), $NBRCS_{area}$ (~ 0.46), Γ_{p_area} (~ 0.46). Based on both, the optimum points of the curves and the area under the curves, E_{fast} shows a behavior almost similar to E_{full}, which confirms the functional relationship found in Fig. 22. The threshold levels (one for each observable) at the optimum operating points of the ROC curves can be used for coherence detection, and thus for inland water bodies tracking. Future versions of this product could include more coherence detectors [57].

6 Conclusions

The new CYGNSS multi-resolution land data product based on enhanced quality DDMs is generated after processing and calibrating raw IF collections. Γ_p times series with low integration times e.g. N_{inc} = 2 ms and 50 ms capture land-water transitions with high accuracy because of the higher signal dynamic range and the higher spatial resolution as compared to the standard mission L1 product. In addition to power observables, the use of complex DDMs allows us to characterize the performance of more advanced algorithms for
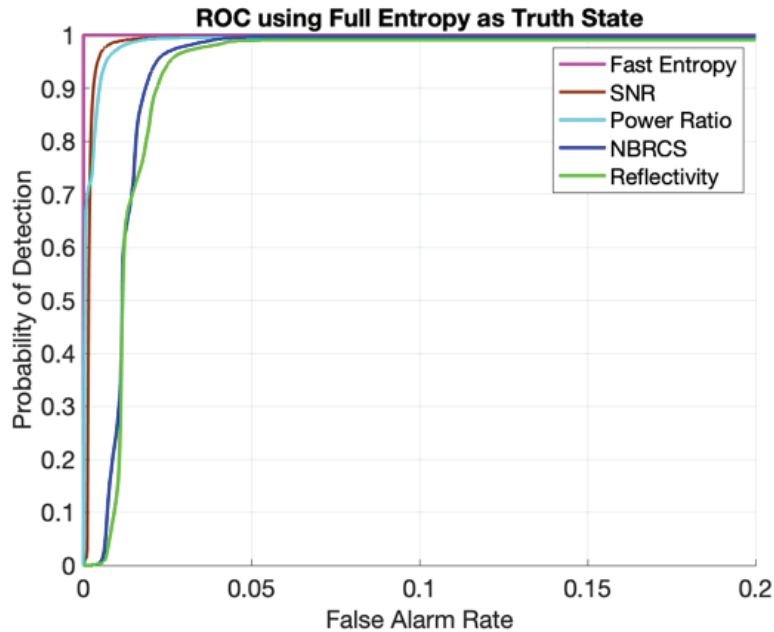
Fig. 23. ROC curves of the peak-observables (SNR, Γ_p, and $NBRCS$) and the coherence detectors (E_{fast} and P_{ratio}) using E_{full} as the truth reference. Entropy detectors with 50 ms of resolution, and the rest of parameters with N_{inc} = 50 ms.

coherence detection. Bistatic scattering regimes are classified in incoherent ($E_{full} \sim > 0.7$), partially coherent ($0.3 \sim < E_{full} \sim < 0.7$), and coherent ($E_{full} \sim < 0.3$) by analyzing time series of φ_{peak}. Based on this truth reference state generated with E_{full}, ROC curves are used to characterize the performance of E_{fast}, SNR, P_{ratio}, $NBRCS$, and Γ_p. A PD higher than ~ 95% for a FAR lower than ~ 5% is found at the optimum points of the ROC curves using all the 2022 raw IF tracks over land surfaces. In particular, E_{fast} appears to be an excellent water detector, showing a clear linear functional relationship with E_{full} under the coherent scattering regime. The lower computational requirement of this detector makes it suitable for in-orbit water monitoring.

The ultimate goal of this document is to show the capabilities of our product to the users for further advancement of the CYGNSS science team investigations over land surfaces, with special interest in inland water bodies monitoring. This is currently a hot research topic with the SWOT mission aiming to resolve ~ 100 m wide rivers and ~ 250 m × 250 m lakes and reservoirs.

Appendix: Quality Flags

Table 8. Per-DDM quality flags 1

Flag	Definition
s_band_powered_up	Set if S-band transmitter is powered up
small_sc_attitude_err	Set if the absolute value of the spacecraft roll is between 1 and 30 degrees, the pitch is between 1 and 10 degrees, or the yaw is between 1 and 5 degrees
large_sc_attitude_err	Set if the absolute value of the spacecraft roll is greater than or equal to 30 degrees, the pitch is greater than or equal to 10 degrees, or the yaw is greater than or equal to 5 degrees
black_body_ddm	Set if the black body load was selected during the DDM sampling period
ddmi_reconfigured	Set if the DDMI was reconfigured during the DDM sampling period
spacewire_crc_invalid	Set if the DDM CRC transmitted from the DDMI to the spacecraft computer was not valid
ddm_is_test_pattern	Set if the DDM is a test pattern generated by the DDMI
channel_idle	Set if this reflectometry channel was not tracking a PRN
low_confidence_ddm_noise_floor	Set if the difference between this DDM noise floor and the previous DDM noise floor is greater than 10 %
sp_over_land	Set if the specular point is over land. Referenced using a map with 0.1 degree lat/lon bins. Coastline features or islands smaller than bin size may not be properly captured
sp_very_near_land	Set if the specular point is within 25 km of land. Referenced using a map with 0.1 degree lat/lon bins
sp_near_land	Set if the specular point is within 50 km of land. Referenced using a map with 0.1 degree lat/lon bins
large_step_noise_floor	Set if the difference between this DDM noise floor and the previous DDM noise floor is greater than 0.24 dB
large_step_lna_temp	Set if the LNA temperature rate of change is greater than 1 Celsious degree per minute
direct_signal_in_ddm	Set if the absolute value of the difference between direct signal code phase and the DDM signal code phase is less than or equal to four
low_confidence_gps_eirp_estimate	Set when there is low confidence in the GPS effective isotropic radiated power estimate
rfi_detected	Set when the kurtosis of the DDM noise floor deviates from pure Gaussian by more than 1.0
brcs_ddm_sp_bin_delay_error	Set if the calculated specular point bin delay row is outside of the valid range. This range is different for specular points over land and ocean. The zero-based valid range is greater than 4 (ocean) / 1 (land)and less than 8 (ocean) / 15 (land)
brcs_ddm_sp_bin_dopp_error	Set if the calculated specular point bin Doppler column is outside of the valid range. This range is different for specular points over land and ocean. The zero-based valid range is greater than 4 (ocean) / 2 (land) and less than 6 (ocean) / 8 (land)
neg_brcs_value_used_for_nbrcs	Set if the BRCS bin used to calculate peak_nbrcs has a negative value
gps_pvt_sp3_error	Cannot calculate GPS SV position/velocity/time from SP3 file
sp_non_existent_error	Specular point does not exist
brcs_lut_range_error	Unable to index into BRCS uncertainty lookup table
ant_data_lut_range_error	Unable to index into antenna data lookup table
bb_framing_error	Insufficient black body data for calibration
fsw_comp_shift_error	Flight software telemetry encoding error of the fsw_comp_delay_shift and fsw_comp_dopp_shift variables. Corrected in FSW version 4.5
low_quality_gps_ant_knowledge	Not enough data is available to properly calibrate the NBRCS for this sample's GPS satellite
sc_altitude_out_of_nominal_range	The spacecraft's altitude is out of nominal altitude range. Nominal altitude is defined as between 490 km to 550 km
anomalous_sampling_period	Set when an anomaly was observed on the CYGNSS or GPS satellite while this sample was taken. These samples have produced data that do not align with typical CYGNSS results. See up to date list at: https://docs.google.com/spreadsheets/d/1AFAZanVGDApLSnJQAAdPfOKoJQs0jnB8ZvIuD1Z5mAc/edit?usp=sharing
invalid_roll_state	The spacecraft's reported roll angle is more than 1 degree from the commanded roll

Table 9. Per-DDM quality flags 2

Flag	Definition
incorrect_ddmi_antenna_selection	The wrong (port or starboard) antenna was selected
high_signal_noise	The signal is in the highest noise group, but there are still some OK noise rows. Samples are suspect, but may contain quality data. Flag only used for land applications
noise_floor_cal_error	The signal is off or is very near the top rows of the full DDM. A proper noise floor cannot be computed. Flag only used for land applications
sp_in_sidelobe	The specular point is in the sidelobe causing low confidence in the antenna gain
negligible_nst_outage	Minor star track outage with negligible impact on attitude knowledge
minor_nst_outage	Minor star track outage with small but acceptable impact on attitude knowledge
fatal_nst_outage	Star track outage with unacceptable impact on attitude knowledge
low_zenith_ant_gain	Zenith antenna gain is less than -6 dB
poor_bb_quality	The distance between the surrounding BB samples > 1350 seconds OR the absolute value of the time to the nearest BB > 350 seconds
poor_quality_bin_ratio	Bin ratio on the nadir or zenith antenna is associated with degraded performance
low_coherency_ratio	The coherency ratio is below 0.1 on a land sample
land_poor_overall_quality	Set if this sample is determined to be of overall poor quality for land applications
sp_over_ocean	Set if the specular point is over ocean. Referenced using a map with 0.1 degree lat/lon bins. Coastline features or islands smaller than bin size may not be properly captured
sp_extremely_near_ocean	Set if the specular point is within 10 km of ocean. Referenced using a map with 0.1 degree lat/lon bins. When this flag is set the reflectivity_peak and ddm_nbrcs are both considered to be of poor quality
sp_very_near_ocean	Set if the specular point is within 25 km of ocean. Referenced using a map with 0.1 degree lat/lon bins. When this flag is set the ddm_nbrcs is considered to be poor quailty, but thereflectivity_peak may still contain good quality data

References

[1] C. Ruf et al., "CYGNSS: Enabling the future of hurricane prediction [remote sensing satellites]," IEEE Geoscience and Remote Sensing Magazine, vol. 1, no. 2, pp. 52-67, 2013, doi: 10.1109/MGRS.2013.2260911

[2] C. Ruf et al., "New Ocean Winds Satellite Mission to Probe Hurricanes and Tropical Convection," Bulletin American Meteorological Society, vol. 97, no. 3, pp. 385–395, 2015, doi: 10.1175/BAMS-D-14-00218.1

[3] C. Chew, and E. Small, "Soil Moisture Sensing Using Spaceborne GNSS Reflections: Comparison of CYGNSS Reflectivity to SMAP Soil Moisture," Geophysical Research Letters, vol. 45, pp. 4049-4057, 2018, https://doi.org/10.1029/2018GL077905

[4] M.P. Clarizia, N. Pierdicca, F. Costantini, N. Floury, "Analysis of CYGNSS Data for Soil Moisture Retrieval," IEEE Journal of Selected Topics in Geoscience and Remote Sensing, vol. 12, no. 7, pp. 2227-2235, 2019, doi: 10.1109/JSTARS.2019.2895510

[5] M.M. Al-Khaldi, J.T. Johnson, S. Gleason, C. Chew, C. Gerlein-Safdi, R. Shah, and C. Zuffada, "Inland Water Body Mapping Using CYGNSS Coherence Detection," IEEE Transactions on Geoscience and Remote Sensing, vol. 59, no. 9, pp. 7385-7394, 2021, doi: 10.1109/TGRS.2020.3047075

[6] J. Zhang, J. Morton, Y. Wang, C. J. Roesler, "Mapping Surface Water Extents Using High-Rate Coherent Spaceborne GNSS-R Measurements," IEEE Transactions on Geoscience and Remote Sensing, vol. 60, no. 4211115, 2022, doi: 10.1109/TGRS.2022.3218254

[7] B. Chapman, I. M. Russo, C. Galdi, M. Morris, M. di Bisceglie, C. Zuffada, B. Downs, M. Lavalle, E. Loria, and A. O'Brien, "Comparison of SAR and CYGNSS Surface Water Extent Metrics," IEEE Journal of Selected Topics in Geoscience and Remote Sensing, vol. 15, pp. 3235-3245, 2022, doi: 10.1109/JSTARS.2022.3162764

[8] H. Carreno-Luengo, and C. Ruf, "Mapping Freezing and Thawing Surface State Periods with the CYGNSS Based F/T Seasonal Threshold Algorithm," IEEE Journal of Selected Topics in Geoscience and Remote Sensing, vol. 16, pp. 9943-9952, 2022, doi: 10.1109/JSTARS.2022.3216463

[9] M. Martin-Neira, "A Passive Reflectometry and Interferometry System (PARIS): Application to Ocean Altimetry," ESA Journal, vol. 17, pp. 331–355, 1993.

[10] J.L. Garrison and S.J. Katzberg, "The Application of Reflected GPS Signals to Ocean Remote Sensing," Remote Sensing of the Environment, vol. 73, no. 2, pp. 175-187, 2000, https://doi.org/10.1016/S0034-4257(00)00092-4

[11] S.T. Lowe, J.L. LaBrecque, C. Zuffada, L.J. Romans, L.E. Young, and G.A. Hajj, "First Spaceborne Observation of an Earth-Reflected GPS Signal," Radio Science, vol. 37, pp. 7–1–7–28, 2002, doi: 10.1029/2000RS002539

[12] A. Camps, "Introduction to Remote Sensing Using GNSS Signals of Opportunity," Ocean Remote Sensing Technologies: High Frequency, Marine and GNSS-Based Radar, IET - Institution of Engineering and Technology, 2021, ISBN-13: 978-1-83953-161-3

[13] V.U. Zavorotny, S. Gleason, E. Cardellach, and A. Camps, "Tutorial on Remote Sensing Using GNSS Bistatic Radar of Opportunity," IEEE Geoscience and Remote Sensing Magazine, vol. 2, no. 4, pp. 8-45, 2014, doi: 10.1109/MGRS.2014.2374220

[14] J. Wickert et al., "GEROS-ISS: GNSS REflectometry, Radio Occultation, and Scatterometry onboard the International Space Station," IEEE Journal of Selected Topics in Geoscience and Remote Sensing, vol. 9, no. 10, pp. 4552-4581, 2016, doi: 10.1109/JSTARS.2016.2614428

[15] E. Cardellach et al., "GNSS Transpolar Earth Reflectometry exploriNg system (G-TERN): Mission concept," IEEE Access, vol. 6, pp. 13980-14018, 2018, doi: 10.1109/ACCESS.2018.2814072

[16] N. Pierdicca, et al., "The Potential of Spaceborne GNSS Reflectometry for Soil Moisture, Biomass, and Freeze–Thaw Monitoring: Summary of a European Space Agency-Funded Study," IEEE Geoscience and Remote Sensing Magazine, vol. 10, no. 2, pp. 8-38, 2021, doi:10.1109/MGRS.2021.3115448

[17] E. Loria, A. O'Brien, and I.J. Gupta, "Detection & Separation of Coherent Reflections in GNSS-R Measurements Using CYGNSS Data," in Proc. of the 2018 IEEE IGARSS, pp. 3995-3998, doi: 10.1109/IGARSS.2018.8517441, Valencia, Spain, July 2018.

[18] W. Li, E. Cardellach, F. Fabra, S, Ribo, and A. Rius, "Assessment of Spacebrone GNSS-R Ocean Altimetry Performance Using CYGNSS Mission Raw Data," IEEE Transactions on Geoscience and Remote Sensing, vol. 58, no. 1, pp. 238-250, 2020, doi: 10.1109/TGRS.2019.2936108

[19] Y. Wang, and J. Morton, "Coherent GNSS Reflection Signal Processing for High-Precision and High-Resolution Spaceborne Applications," IEEE Transactions on Geoscience and Remote Sensing, vol. 59, no. 1, pp. 831-842, 2021, doi: 10.1109/TGRS.2020.2993804

[20] A. Warnock and C. Ruf, "Response to Variations in River Flowrate by a Spaceborne GNSS-R River Width Estimator," MDPI Remote Sensing, vol. 11, no. 20, pp. 2450, 2019, https://doi.org/10.3390/rs11202450

[21] Y. Wang and J. Morton, "River Slope Observations from Spaceborne GNSS-R Carrier Phase Measurements: A Case Study", IEEE Geoscience and Remote Sensing Letters, vol. 19, no. 1503105, 2021, doi: 10.1109/LGRS.2021.3127750

[22] S.V. Nghiem, C. Zuffada, R. Shah, C. Chew, S.T. Lowe, A.J. Mannucci, E. Cardellach, G.R. Brakenridge, G. Geller, and A. Rosenqvist, "Wetland Monitoring with Global Navigation Satellite System Reflectometry," AGU Earth and Space Science, vol. 4, no. 1, pp. 1-24, 2017, https://doi.org/10.1002/2016EA000194

[23] B. Downs, A.J. Kettner, B.D. Chapman, G.R. Brakenridge, A.J. O'Brien, and C. Zuffada, "Assessing the Relative Performance of GNSS-R Flood Extent Observations: Case Study in South Sudan," IEEE Transactions on Geoscience and Remote Sensing, vol. 61, no. 4201213, 2023, doi: 10.1109/TGRS.2023.3237461

[24] A. Camps, H. Park, J. Castellví, J. Corbera, E. Ascaso, "Single-Pass Soil Moisture Retrievals Using GNSS-R: Lessons Learned" MDPI Remote Sensing, vol. 12, no. 12, pp. 2064, 2020, https://doi.org/10.3390/rs12122064

[25] H. Carreno-Luengo, A. Warnock, and C. Ruf, "The CYGNSS Coherent End-to-End Simulator: Development and Results," in Proc. of the 2022 IEEE IGARSS, pp.7441-7444, doi: 10.1109/IGARSS46834.2022.9884499, Kuala Lumpur, Malaysia, July 2022.

[26] J. Campbell et al., "Intercomparison of Electromagnetic Scattering Models for Delay-Doppler Maps along a CYGNSS Land Track with Topography" IEEE Transactions on Geoscience and Remote Sensing, vol. 60, no. 2007413, 2022, doi:10.1109/TGRS.2022.3210160

[27] M. Unwin et al., "An introduction to the HydroGNSS GNSS Reflectometry Remote Sensing Mission," IEEE Journal of Selected Topics in Geoscience and Remote Sensing, vol. 14, pp. 6987-6999, 2021, doi: 10.1109/JSTARS.2021.3089550

[28] H. Carreno-Luengo, and A, Camps, "First Dual-Band Multi-Constellation GNSS-R Scatterometry Experiment over Boreal Forests from a Stratospheric Balloon," IEEE Journal of Selected Topics in Geoscience and Remote Sensing, vol. 9, no. 10, pp. 4743-4751, 2015, doi: 10.1109/JSTARS.2015.2496661

[29] H. Carreno-Luengo, and A. Camps, "Unified GNSS-R Formulation Including Coherent and Incoherent Scattering Components," in Proc. of the 2016 IEEE IGARSS, pp. 4815-4818, doi: 10.1109/IGARSS.2016.7730256, Beijing, China, July 2016.

[30] A. Camps, "Spatial Resolution in GNSS-R Under Coherent Scattering", IEEE Geoscience and Remote Sensing Letters, vol. 17, no. 1, pp. 32-36, 2019, doi: 10.1109/LGRS.2019.2916164

[31] H. Carreno-Luengo, C. Ruf, A. Warnock, and K. Brunner, "Investigating the Impact of Coherent and Incoherent Scattering Terms in GNSS-R Delay Doppler Maps," in Proc. of the 2020 IEEE IGARSS, pp. 6202-6205, doi: 10.1109/IGARSS39084.2020.9324404, Hawaii, USA, July 2020.

[32] E. Loria, A. O'Brien, V. Zavorotny, B. Downsa, and C. Zuffada, "Analysis of Scattering Characteristics from Inland Bodies of Water Observed by CYGNSS," Remote Sensing of the Environment, vol. 245, no. 111825, 2020, https://doi.org/10.1016/j.rse.2020.11182

[33] H. Carreno-Luengo, C. Ruf, S. Gleason, A. Russel, and T. Butler, "Generation of a New High Resolution DDM Data Product from CYGNSS Raw IF Measurements," in Proc. of the 2021 IEEE IGARSS, pp.7815-7818, doi: 10.1109/IGARSS47720.2021.9554828, Brussels, Belgium, July 2021.

[34] H. Carreno-Luengo, A. Camps, N. Floury, M. Martin-Neira, C. Ruf, T. Wang, S.-J. Khalsa, M. P. Clarizia, J. Reynolds, J. Johnson, A. O'Brien, C. Galdi, M. di Bisceglie, A. Dielacher, P. Jales, M. Unwin, L. King, G. Foti, R. Shah, D. Pascual, B. Schreiner, M. Asgarimehr, J. Wickert, S. Ribo, and E. Cardellach, "IEEE Standard for Global Navigation Satellite System-Reflectometry (GNSS-R) Data and Metadata Content," IEEE Standards Association, 2021, doi: 10.1109/IEEESTD.2021.9594781

[35] S. Gleason, "Level 1A DDM Calibration Algorithm Theoretical Basis Document," CYGNSS Project Document 148-0136, Rev 2, 20 Aug. 2018.

[36] S. Gleason, and D. Gebre-Egziabher (editors), "GNSS Applications and Methods," Artech House, 2009, ISBN 978-1-59693-329-3.

[37] P. Jales, "Spaceborne Receiver Design for Scatterometric GNSS Reflectometry, PhD Thesis, University of Surrey, 2015.

[38] S. Gleason, C.S. Ruf, M.P. Clarizia, and A. O'Brien, "Calibration and Unwrapping of the Normalized Scattering Cross Section for the Cyclone Global Navigation Satellite System," IEEE Journal of Selected Topics in Geoscience and Remote Sensing, vol. 54, no. 5, pp. 2495-2509, 2016, doi: 10.1109/TGRS.2015.2502245

[39] S. Gleason, C.S. Ruf, A. O'Brien, and D. McKague, "The CYGNSS Level 1 Calibration Algorithm and Error Analysis Based on On-Orbit Measurements," IEEE Journal of Selected Topics in Geoscience and Remote Sensing, vol. 12, no. 1, pp. 37-49, 2018, doi: 10.1109/JSTARS.2018.2832981

[40] S. Gleason, A. O'Brien, A. Russel, M. Al-Khaldi, and J.T. Johnson, "Geolocation, Calibration and Surface Resolution of CYGNSS GNSS-R Land Observations," MDPI Remote Sensing, vol. 12, no. 8, pp. 1317, 2020, doi:10.3390/rs12081317.

[41] C. Powell, C.S. Ruf, and A. Russel, "An Improved Blackbody Calibration Cadence for CYGNSS," IEEE Transactions on Geoscience and Remote Sensing, vol. 60, 2022, doi: 10.1109/TGRS.2022.3165001

[42] M. Zribi, K. Dassas, V. Dehaye, P. Fanise, E. Ayari, and M. Le Page, "Analysis of Polarimetric GNSS-R Airborne Data as a Function of Land Use," IEEE Geoscience and Remote Sensing Letters, vol. 20, no. 2502105, 2023, doi: 10.1109/LGRS.2023.3270730

[43] A. Egido S. Paloscia, E. Motte, L. Guerriero, N. Pierdicca, M. Caparrini, E. Santi, G. Fontanelli, and N. Floury, "Airborne GNSS-R Polarimetric Measurements for Soil Moisture and Above-Ground Biomass Estimation," Journal of Selected Topics in Geoscience and Remote Sensing, vol. 7, no. 5, pp. 1522-1532, 2014, doi: 10.1109/JSTARS.2014.2322854

[44] E. Santi, et al., "Remote Sensing of Forest Biomass Using GNSS Reflectometry," IEEE Journal of Selected Topics in Geoscience and Remote Sensing, vol. 13, pp. 2351-2368, 2020, doi: 10.1109/JSTARS.2020.2982993

[45] S. Gleason, "Remote Sensing of Ocean, Ice and Land Surfaces Using Bistatically Scattered GNSS Signals from Low Earth Orbit," PhD Thesis, University of Surrey, 2006.

[46] I. M. Russo, M. di Bisceglie, C. Galdi, M. Lavalle, and C. Zuffada, "Entropy-Based Coherence Metric for Land Applications of GNSS-R," IEEE Transactions on Geoscience and Remote Sensing, vol. 60, no. 5613413, 2021, doi: 10.1109/TGRS.2021.3125858

[47] S. Andrilli and D. Hecker, "Elementary Linear Algebra," Elsevier, 2010, https://doi.org/10.1016/C2009-0-19744-1

[48] M.M. Al-Khaldi, J.T. Johnson, S. Gleason, E. Loria, A.J. O'Brien, and Y. Yi, "An Algorithm for Detecting Coherence in Cyclone Global Navigation Satellite System Mission Level-1 Delay-Doppler Maps," IEEE Transactions on Geoscience and Remote Sensing, vol. 59, no. 5, pp. 4454-4463, 2021, doi: 10.1109/TGRS.2020.3009784

[49] J.F. Pekel, A. Cottam, N. Gorelick, and A.S. Belward, "High-Resolution Mapping of Global Surface Water and its Long-Term Changes," Nature, vol. 540, no. 7633, pp. 418-422, 2016, doi:10.1038/nature20584

[50] E. Motte, M. Zribi, P. Fanise, A. Egido, J. Darrozes, A. Al-Yaari, N. Baghdadi, F. Baup, S. Dayau, R. Fieuzal, et al., "GLORI: A GNSS-R Dual Polarization Airborne Instrument for Land Surface Monitoring," MDI Sensors, vol. 16, no. 5, pp. 732, 2016, https://doi.org/10.3390/s16050732

[51] A.G. Voronovich and V.U. Zavorotny, "Bistatic Radar Equation for Signals of Opportunity Revisited," IEEE Transactions on Geoscience and Remote Sensing, vol. 56, no. 4, pp. 1959-1968, 2017, doi: 10.1109/TGRS.2017.2771253

[52] N. Pierdicca, L. Guerriero, R. Giusto, M. Brogioni, and A. Egido, "SAVERS: A Simulator of GNSS Reflections from Bare and Vegetated Soils," IEEE Transactions on Geoscience and Remote Sensing, vol. 52, no. 10, pp. 6542-6554, 2014, doi: 10.1109/TGRS.2013.2297572

[53] D. Comite, F. Ticconi, L. Dente, L. Guerriero, and N. Pierdicca, "Bistatic Coherent Scattering from Rough Soils with Application to GNSS Reflectometry," IEEE Transactions on Geoscience and Remote Sensing, vol. 58, no. 1, pp. 612–625, 2020, doi: 10.1109/TGRS.2019.2938442

[54] L. Dente, L. Guerriero, D. Comite, and N. Pierdicca, "Space-borne GNSS-R Signal over a Complex Topography: Modeling and Validation," IEEE Journal of Selected Topics in Geoscience and Remote Sensing, vol. 13, pp. 1213-1218, 2020, doi: 10.1109/JSTARS.2020.2975187

[55] M. Morris, C. Chew, J. T. Reager, R. Shah, and C. Zuffada, "A Novel Approach to Monitoring Wetland Dynamics Using CYGNSS: Everglades Case Study," Remote Sensing of the Environment, vol. 233, no. 111417, 2019, https://doi.org/10.1016/j.rse.2019.111417

[56] C. Gerlein-Safdi, A.A. Bloom, G. Plant, E.A. Kort, and C.S. Ruf, "Improving Representation of Tropical Wetland Methane Emissions with CYGNSS Inundation maps," AGU Global Biogeochemical Cycles, vol. 35, no. 12, pp. e2020GB006890, 2021, https://doi.org/10.1029/2020GB006890

[57] E. Loria, I.M. Russo, Y. Wang, G. Giangregorio, C. Galdi, M. di Bisceglie, B. Wilson-Downs, M. Lavalle, A.J. O'Brien, J. Morton, and C. Zuffada, "Comparison of GNSS-R Coherent Reflection Detection Algorithms Using Simulated and Measured CYGNSS Data," IEEE Transactions on Geoscience and Remote Sensing, vol. 61, 2023, doi: 10.1109/TGRS.2023.3277411